Synthesis of metallic oxide nanoballs via submerged glow-discharge plasma and their photocatalytic effect

Muhammad Rafiq Mirza bin Julaihi

Division of Quantum Science and Engineering

Graduate School of Engineering,

Hokkaido University

March 2015

Contents

Chapter 1 Introduction

Chapter 1 Introduction

Submerged glow-discharge plasma has been researched as a method of nanoparticles (nanoballs) synthesis method [1-3]. The discovery of formation of metallic nanoballs during plasma electrolysis has been documented [2-7]. The product that was obtained from the electrolyte plasma electrolysis was found to be uniformly-shaped spherical particles called “nanoballs” [6, 7-11].

During formation of nanoballs, some of the particles’ surfaces were oxidized because of the high temperature environment or exposure to air after plasma treatment. Ti nanoballs in particular were found to have TiO_2 surface layers. Since TiO_2 is a photocatalytic material, the research aims to characterize the metallic nanoballs in terms of their photocatalytic performance. Also, one possible industrial application of the metallic nanoballs is photocatalytic materials. Using submerged glow-discharge plasma, photocatalytic nanoballs can be synthesized easily and inexpensively as demand for new photocatalytic materials increase.

As a result of glow-discharge plasma layer acting on the surface of the cathode, which has very high temperature, melted nanoparticles was released from the cathode. As they enter the liquid region, they solidify into spherical nanoballs because of the surface tension of the electrolyte and the natural tendency to assume spherical shape. These nanoballs were found to have photocatalytic ability when irradiated with UV-light. Other than semiconductor materials such as TiO_2 and ZnO nanoballs, SUS316L nanoballs which are not semiconductor materials were found to have

photocatalytic ability as well [3].

Glow-discharge region was chosen as the method for nanoballs synthesis because the predictability and ease of control of glow-discharge plasma. The advantages of submerged glow-discharge plasma for nanoballs synthesis are: (1) simple experimental setup, (2) ease of control of nanoball sizes, (3) ease of mass production because of relatively high yield, and (4) use of easily available metallic wires as raw materials for nanoballs synthesis.

Other materials that can be synthesized via submerged glow-discharge plasma include virtually all metallic elements and alloys. As long as glow-discharge plasma can be sustained using a particular metallic electrode, nanoballs can be obtained from that particular metal. Types of metallic nanoballs that have been successfully synthesized include stainless steel, zinc, titanium, gold, nickel, silver and platinum [28-34].

Examples of photocatalytic materials are titanium dioxide [35-44] and zinc oxide [51-62]. In this research, materials that are not semiconductors such as stainless steel nanoballs have been found to have photocatalytic effect. The advantage of stainless steel nanoballs as a photocatalyst is that it reduces wastage of scrap steel and converts them into a useful product.

Previous researches described the use of stainless steel as support for gold-catalysts [63-64]. Usage of stainless steel as support for other types of catalysts have also been documented [65-66], however usage of stainless steel as a photocatalyst material itself has not been studied yet.

This research also aims to demonstrate the ability of stainless steel nanoballs as a photocatalytic material and the difference in the decomposition pathway of methylene blue (MB) in stainless steel.

MB dye was chosen as the indicator of photocatalytic performance because its decomposition pathway has been extensively documented in scientific literature and thus well-understood [60, 91-99]. Based on its use in the scientific community, especially in the photocatalytic materials field, it is a suitable material to be used as a representative of the pollutants that exists in water.

1.1 Plasma processing as a method of nanoparticles production

Since this research focuses on submerged glow-discharge plasma as the synthesis method, other types of plasma processing has also been considered. Those methods are arc-discharge [12], chemical vapor deposition (CVD), gas-phase [13-16] and liquid phase methods [17-20]. Besides plasma processing, chemical and thermal methods such as sol-gel and hydrothermal methods were also examined.

Arc-discharge method requires a very high temperature and a gas chamber, since gas supply is needed to sustain the arc-discharge. This method was shown to produce spherical nanoparticles. Also, this method allows for the synthesis of highly pure nanoparticles with very low contaminants. However, the difficulty in experimental setup means a simpler method is preferable. CVD also requires a very high temperature (>2000°C) and a gas supply to synthesize nanoparticles. It also shares the same merits as arc-discharge method. However, a substrate material is necessary as the method sputters molten material onto a target [12, 21-22]. This limits the form of the end product and therefore its usage.

Gas-phase plasma methods are able to produce high purity nanoparticles [12, 15]. However, but they require high temperatures and the usage of chloride gas and a vacuum chamber. This makes it difficult to collect the nanoparticles after synthesis and there is the need to evacuate chlorine gas safely.

Liquid-phase plasma methods are able to produce highly dispersive nanoparticles at low temperatures. This is achieved by chemical reduction

of the solvent. However, this method requires a reducing agent and it takes a long time to grow the nanoparticles [19, 20].

Sol-gel process is able to synthesize multicomponent nanoparticles and it has high controllability. Therefore this method is suitable if a high degree of customization is required. The main disadvantage of sol-gel process is that it needs many chemicals and reagents. Furthermore, sol-gel process requires numerous steps in order to successfully synthesize the desired end product. Therefore sol-gel process is time-consuming and rather uneconomical.

Hydrothermal process is much simpler than sol-gel process although this reduces the controllability. Hydrothermal process has the drawback of requiring a lot of energy. This is to ensure the reactions involved can be initiated and sustained for the whole duration of the nanoparticles synthesis. Also, the synthesized end product must be separated from the rest of the leftover reactants. This adds further steps before being able to use the product.

Based on the merits and demerits of the processes above, submerged glow-discharge plasma was chosen as the method for synthesis of nanoballs. This is because of the ease of setup and voltage control. Also, the plasma that appears during glow-discharge is predictable and easily controlled via voltage control, unlike arc-discharge which is violent and turbulent. There was no need to supply gas, unlike arc-discharge method. The resulting product can be separated easily from the electrolyte via simple centrifuging.

1.2 Submerged glow-discharge plasma

1.2.1 Basics of glow discharge plasma

For glow discharge in a gaseous medium, noble gas such as argon or neon is filled in a tube-like vessel that includes two electrodes (anode and cathode), such as shown in Figure 1-1. Glow discharge occurs if the proper voltage in applied between the electrodes. This is the simplest type of glow discharge and has been examined as one of the basic type of discharges by many researchers. “Aston dark space” that results from the secondary electron nearby the cathode, which is emitted from the cathode by positive-ion bombardment, is not accelerated much and its energy is too low to excite neutral atoms by collision. In “cathode dark space”, the energy of the secondary electron exceeds the excitation energy for neutral atom and only ionization occurs.

The positive ion bursts into the cathode is generated within the cathode dark space. The strong electric field caused by the steep cathode voltage-drop is weakened at the end of the cathode dark space. This leads to energy decrease of the electron to a level fit for excitation. In “negative glow”, excitation occurs again and also recombination with positive ion comes from anode-side. No light is emitted in “Faraday dark space” because the electron has lost its energy and its mean magnitude is not enough for enough for both excitation and ionization to occur.

The electric field is strengthened again at “Faraday dark space”, and then light from the recombination is also decreased. When electron goes through the “positive column”, the electron is accelerated again and the

light from excitation is emitted. The “positive column” is mostly in neutral state.

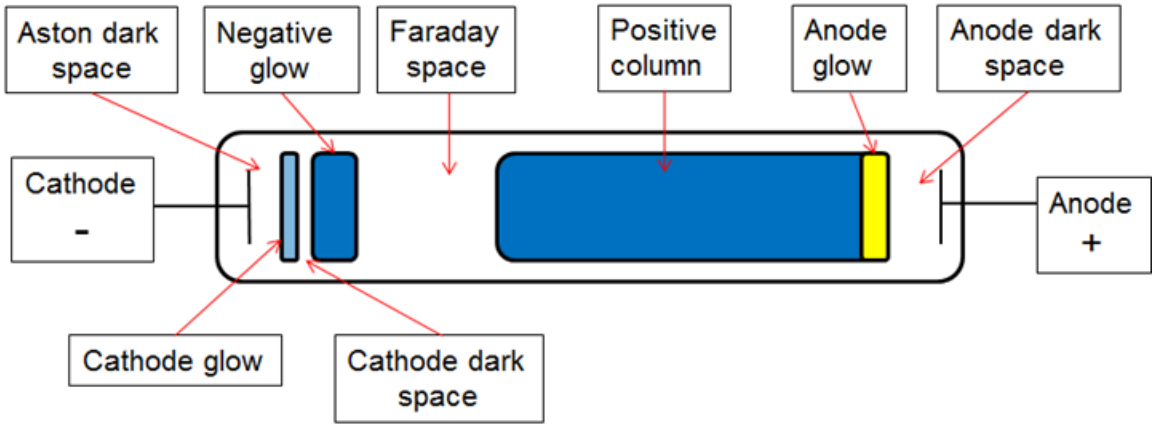

Figure 1-1 Sketch of a glow discharge tube. The characterization at each part of the tube is explained in the above section.

The main stages are:

1) Dark discharge, including Townsend discharge

2) Glow discharge

3) Arc discharge

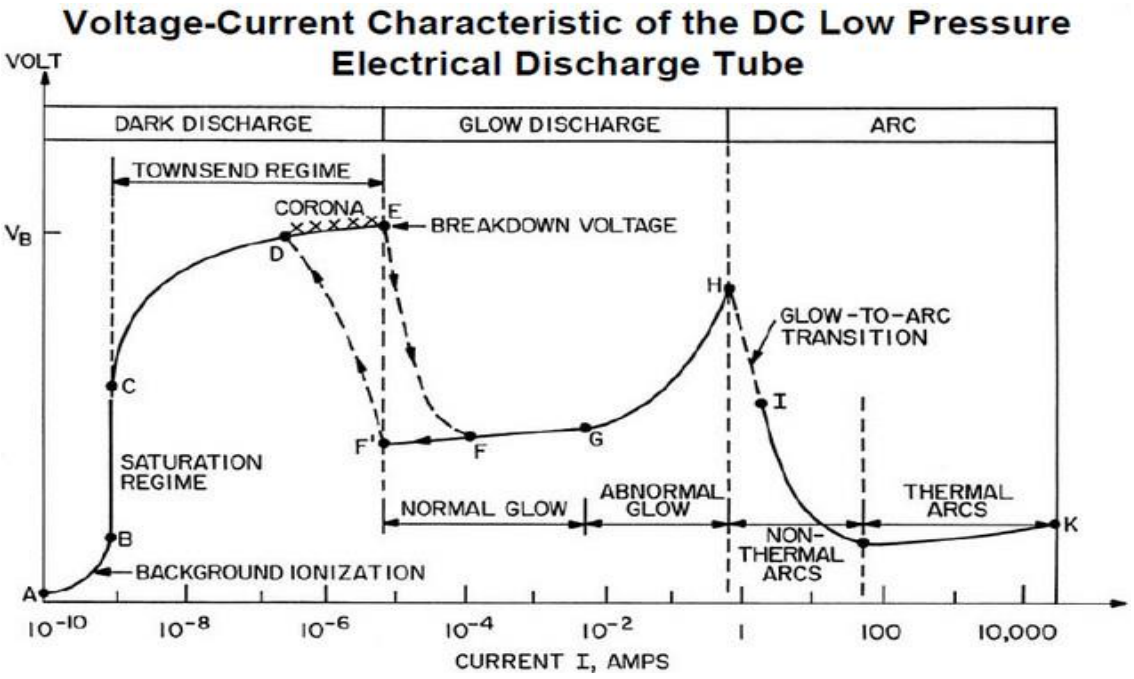

Figure 1-2 Voltage –current characteristics of low pressure plasma discharges [52].

Figure 1-2 shows the voltage-current characteristics of low pressure plasma discharge. In dark discharge stage, the discharge is not visible except in corona and breakdown. In this stage, the discharge is not self-sustaining. In the background ionization stage (A-B), the electric field applied along the axis of the discharge tube sweeps out the ions and electrons created by the ionization from background radiation. In the saturation region (B-C), the current remains constant when the voltage is raised. The Townsend discharge (C-E) is a gas-ionization process where an

initially small amount of free electrons are accelerated by a sufficiently strong electric field until their energy is higher than the ionization potential so that they can ionize neutral atoms. With the increase of electric field strength, the electron from these neutral atoms can ionize other neutral atoms, which then gives rise to electrical conduction through the gas via avalanche multiplication. The corona discharge at D-E region happens before the electrical breakdown. If the current is high enough, corona discharge is visible. However for low current case, the entire corona is dark. Electrical breakdown (E) occurs with the emitting of secondary electrons from the cathode caused by ion impact to the cathode surface. The breakdown voltage for some gas and electrode material depends on the product of the pressure and the distance between the electrodes, as expressed in Paschen's Law [1].

Plasma is luminous in the glow discharge stage. The gas glows as the energy and density of the electron are high enough to generate light by excitation collisions. In this stage the discharge is self-sustaining. After the transition from electrical breakdown (E-F), the gas enters the normal glow region. The voltage here is independent of the increasing current. As the current rise, the fraction of the cathode occupied by plasma increases until all cathode surfaces is covered by plasma. In this stage, positive ions are accelerated to the cathode and collide with cathode surface, which then emit secondary electron. This secondary electron will then accelerate in the plasma and ionizes neutral atoms. The process repeats, causing the plasma to become self-sustaining. In the abnormal glow discharge stage (G-H),

with the increase of current, the voltage also increases.

In the arc discharge stage (H-K), the electrodes become so hot that the cathode emits electrons thermionically. Consequently, the voltage decreases while the current increases. When the cathode starts melting, the voltage increases again.

Slow positive ions attracted by the cathode collide with the cathode surface, releasing secondary electrons. One of these secondary electrons gets accelerated in the electric field, colliding with neutral atoms producing *m* number of electrons and *m* number of positive ions through ionization in the gas on its path to anode. The formula for self-sustaining is:

$$m\gamma=1$$

where γ is number of secondary electrons for each positive ion striking the cathode, and m is ion multiplication factor.

1.2.2 Nanoparticles production using submerged glow-discharge plasma

In the electrolysis stage, with the increase of input voltage, the current also rises. With constant voltage, the change of electrolyte temperature nearby the cathode or polarization state can change the value of the current. In the vaporization point, cathode temperature increases to electrolyte boiling point so that water vapor is generated. Water vapor surrounds the cathode, which creates a thin gas layer. Since the conductivity of this gas layer is low compared to electrolyte conductivity and the electrolyte departs from the cathode, the current drops as the cell voltage increases. In the transition stage, the more the voltage increases, the more cathode surface is covered with gas layer, then the current decreases.

In the localized plasma stage, the cathode surface area that is covered with the thin gas layer that expands continuously, and covering all surface area is established at the end of this stage. On the other hand, in this stage, continuous (self-sustainable) ionization begins partly inside the gas layer as the cell voltage increases. This means continuous gaseous discharge has started. From this stage light emission can be seen, although flickering light appears from the behavior of the gas layer and electric current. While the plasma is created in some ways locally, other points on the surface are still in transition stage, so that the current decreases while cell voltage increases. The start of localized plasma stage is subjected to Paschen's law [1]. The law shows that the breakdown voltage (spark voltage) at the start plasma formation depends only on the product of gas

layer thickness and pressure, while the dependency on the electrolyte material or concentration is very small. With the increase of voltage, the localized plasma spreads until all cathode surfaces are covered with a plasma layer. The more the voltage is raised, the more discharge stage progresses and spark plasma appears, increasing cathode temperature. This may show the stage of abnormal glow discharge or arc discharge.

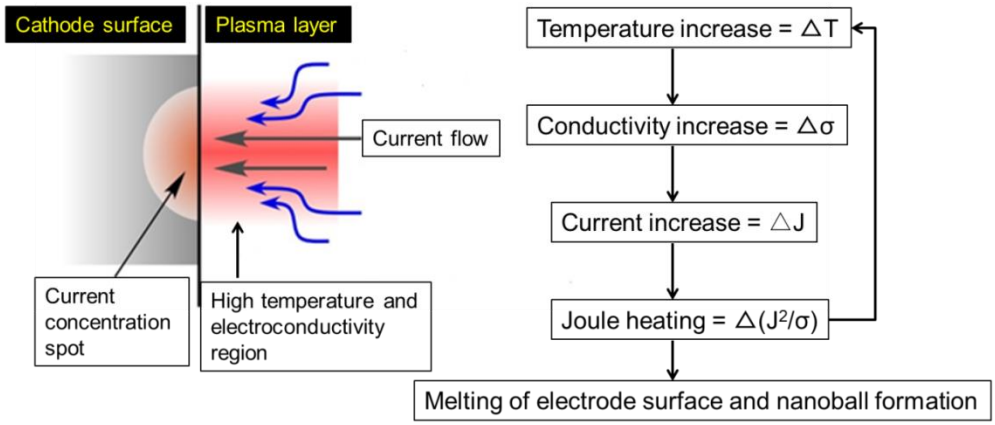

Figure 1-3 Mechanism of nanoball formation due to the electrothermal instability of plasma layer

Figure 1-3 shows the mechanism of the formation of nanoballs during submerged glow-discharge plasma experiment. Nanoballs are formed when current concentration effect occurs on the cathode surface caused by the electro thermal instability in the submerged glow discharge plasma. Macroscopically, in constant discharge state, electric current flowing onto the cathode surface is almost uniform at every surface. Microscopically, the surface has stereoscopic structure rather than planar structure so that the current flows into differently at every spot. In submerged glow- discharge, the gas layer created at the nearby cathode moves upward, thereby not preserving the layer's thickness and pressure,

so that the distribution of electric current density is formed on the cathode surface and its distribution changes temporally. If the electric current density at one spot of the surface becomes higher than those in the surrounding area even for a moment, Joule heating at that point also exceeds others. Joule heating raises the plasma temperature at that point up to higher temperature compared with temperature around there. On the other hand, electrical conductivity of such plasma is strongly dependent on temperature. Therefore conductivity also increases much more extent at that point and it leads to increase of current density at that point.

Figure 1-4 shows the results obtained in the research on submerged glow-discharge plasma for nanoparticles production [7]. The number in both figures indicates each stage of discharge. Its ascending sequence from 1 to 5 corresponds to the range from the extreme left to right in the figure below. Nanoballs are synthesized in the plasma region, corresponding to regions 4 and 5.

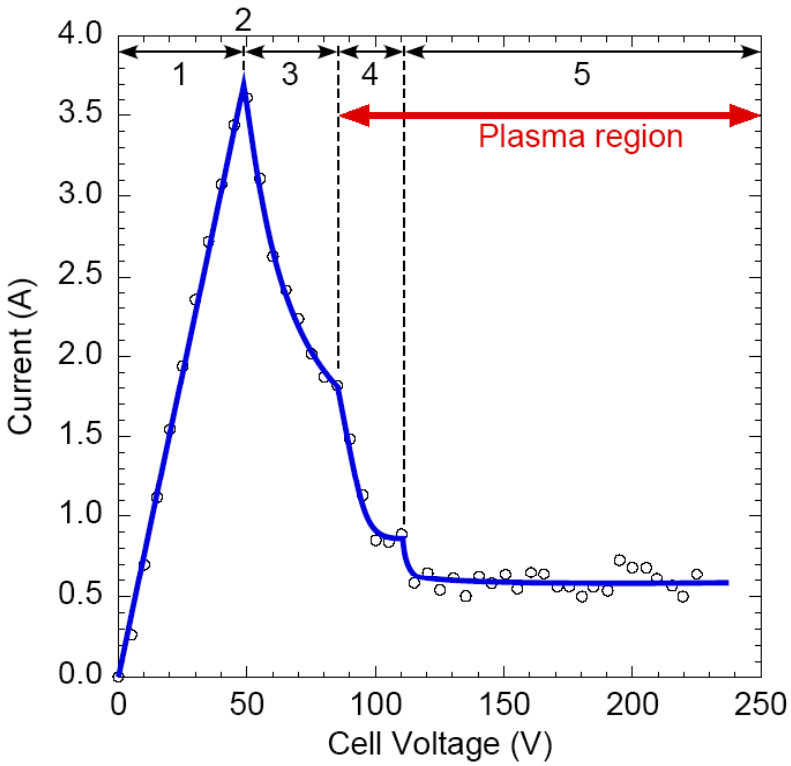

Figure 1-4 Graph showing the relationship between cell voltage, electrical current, and electrolyte temperature of submerged glow-discharge plasma.

Figure 1-5 shows the typical plasma discharge stages occurring during submerged glow-discharge experiment on a Ni cathode. On the extreme left, no electric current is applied to the cathode. As electric current is applied and the voltage is increased, the cathode begins to illuminate. At first the illumination is weak when the voltage is still low. As the voltage is increased further, the illumination becomes stronger until glow-discharge plasma appears in Figure 1-5 (a). When the voltage is increased further, arc-discharge plasma is generated. The cathode then melts almost immediately. This is shown in Figure 1-5 (b), where the Ni cathode glows red and the exposed portion melted.

Although arc-discharge plasma is able to synthesize nanoballs, it

cannot be sustained for a long time. Furthermore, arc-discharge plasma tends to melt the working electrode rapidly. Since glow-discharge plasma is weaker than arc-discharge, it can be sustained for much longer. Therefore glow-discharge plasma is used to synthesize nanoballs.

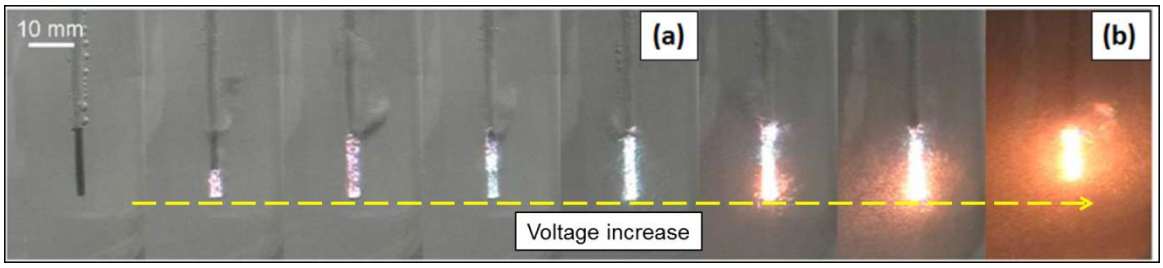

Figure 1-5 Submerged plasma discharge using Ni cathode showing (a) glow-discharge and (b) arc-discharge.

Figure 1-6 shows the typical voltage-current graphs for the type of metals used in this research. The glow-discharge voltage for nanoballs production differs depending on the elements; harder elements require higher voltages to initiate glow-discharge. Based on the voltage-current graphs below, the ideal voltage for nanoballs synthesis can be predicted for maximum nanoball yield.

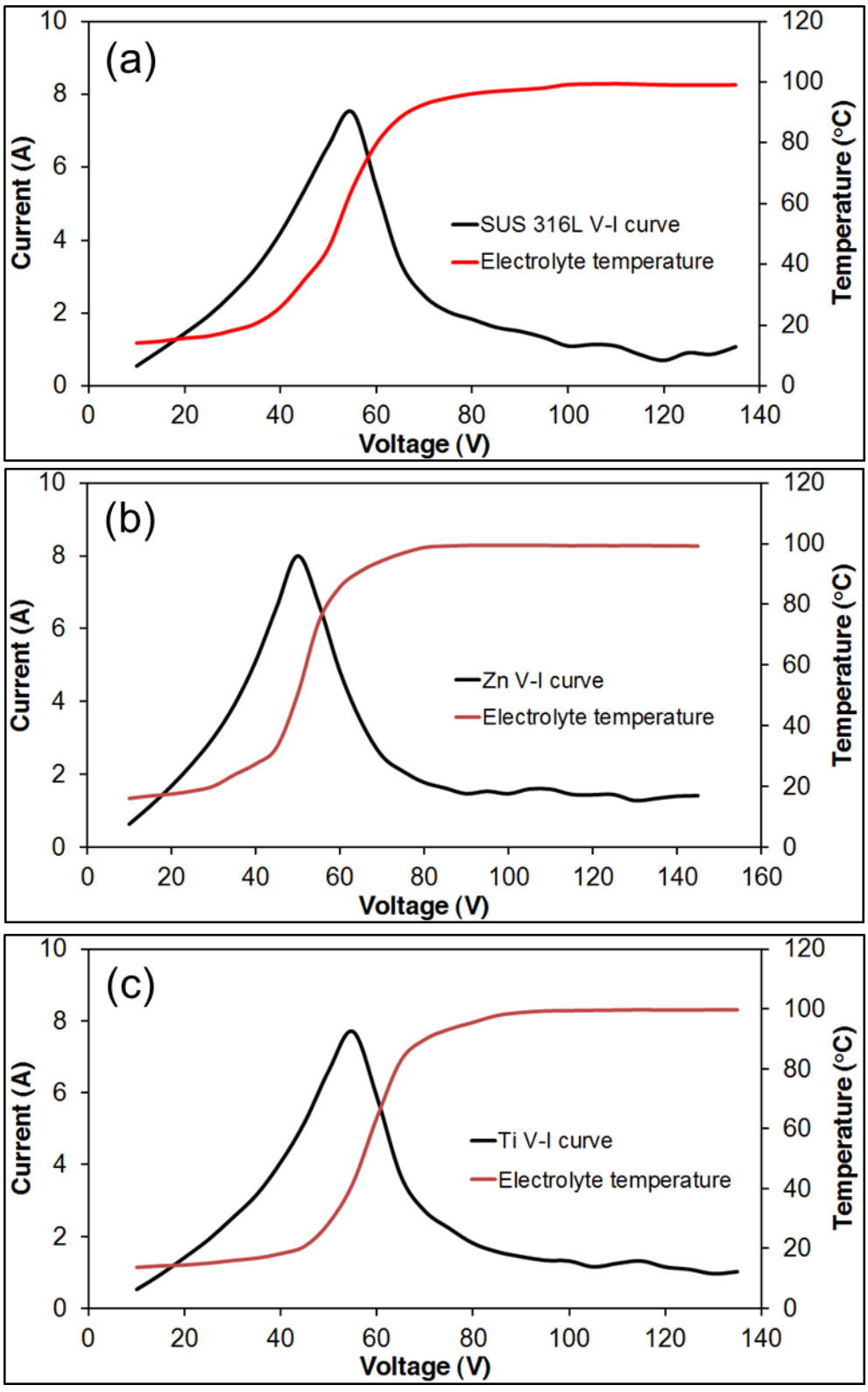

Figure 1-6 Voltage-current curves for glow-discharge plasma for (a) SUS316L, (b) Zn and (c) Ti wires.

1.3 Photocatalytic nanoparticles

1.3.1 Methods of synthesis and usage

Submerged glow-discharge plasma was shown to be a viable method to synthesize oxide nanoballs. However, there has been a lack of effort in determining the potential application of the nanoballs. Since they are nanosized, its properties are different that its bulk form. Nanosized materials are more reactive, for example, gold nanoparticles exhibit catalytic properties and emit different colors depending on their size. Therefore it is clear that these nanoballs should be used as a functional material.

One attractive usage for those nanoballs is as photocatalytic material. Titanium dioxide (TiO_2) is a semiconductive material which has been applied in many industrial applications. It has been used as a pigment, powder for cosmetics, as well as a photocatalyst working under UV light [35-44]. When illuminated with UV light, an electron is promoted from the valence band to the conduction band of TiO_2 to produce an electron-hole pair. Radicals, especially hydroxyl radicals are produced when reacting with water molecules, since the positive hole has a high oxidative potential [35]. The hydroxyl radicals are powerful oxidizers because the electron-hole pair recombine much more slowly than other reactions. Since it is a strong oxidizer, it has been used widely for environmental applications. These include air purification, water purification, antifog mirrors, self-cleaning tiles and self-sterilizing operating theater floor tiles [45-50].

1.3.2 Mechanism of photocatalysis

This section outlines the mechanism of photocatalysis occurring on the surface of a photocatalytic material. The path travels by electron around a nucleus is called “orbit”. There is a limit numbers of electrons can occupy an orbit. Electrons that occupy the outermost orbit are referred as “valence electrons” which responsible for atomic bonding [35]. When number of bonded atoms increases, the values become continuous at certain range known as “energy band”. The one with the highest energy level is “valence band” and band outside of this is “conduction band”. The energy gap between valence band and conduction band is called “band gap”. Amount of energy required by electrons to jump from valence band to conduction band is “band gap energy”.

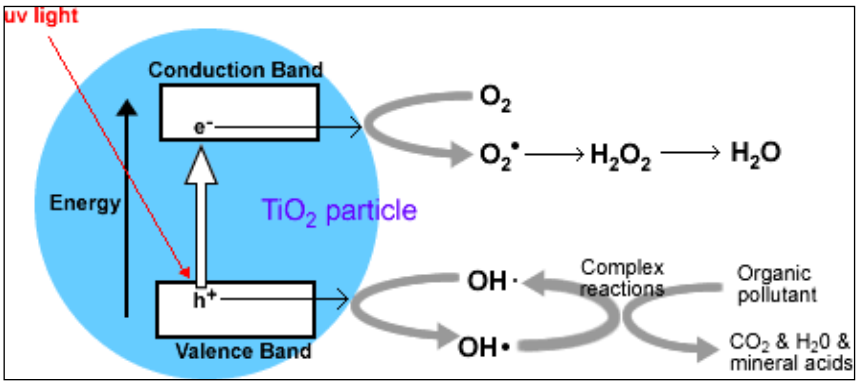

Figure 1-7 Schematic diagram of photocatalytic reaction occurring on the surface of a TiO_2 semiconductor [35].

As shown in Figure 1-7, semiconductors have a band gap; a void region from the top of the filled valence band to the bottom of the vacant conduction band. Because of this void energy region, semiconductors have no energy levels to promote recombination of an electron and a hole

produced by photoactivation in the solid [35]. Eq. (1)-(3) show the steps in the photoelectrochemical reaction. For photoexcitation to occur in order to promote an electron from the valence band to the conduction band, the light energy has to be greater than the band gap to create an electron vacancy or "hole" (h^+) at the valence band edge.

Semiconductor + $h\nu$ ($>E_{bg}$) → (e^-, h^+) (Eq. 1)

$h^+ + Red \rightarrow Red^+$ (Eq. 2)

$e^- + Ox \rightarrow Ox^-$ (Eq. 3)

For light-induced charge separation to happen there must be a depletion layer at the interface between a bulk semiconductor and a liquid medium. The local electrostatic filled present in the space charge layers serves to separate the electron-hole pairs generated by the illumination of the semiconductor. Hence, photoexcitation will generate an electron-hole pair poised at the conduction band and valence band edges. This activated pair component is capable of reducing and oxidizing a surface-adsorbed substrate.

The photogenerated hole can react with an adsorbed substrate by interfacial electron transfer when it reaches the surface of the semiconductor if the adsorbate has enough redox potential for thermodynamic action to occur. Thus, an adsorbed electron donor or reducing agent (Red) can be oxidized by transferring an electron to photogenerated hole on the surface and the oxidizing agent (Ox) or electron acceptor, can be reduced to accept an electron from the surface. From equation (2), cation radical Red^+ will be generated by hole trapping and

from equation 3), an anion radical Ox^- will be generated by electron trapping.

In oxidation mechanism, positive holes (h^+) have a very strong oxidative power that can cause oxidation reaction. They directly oxidize water and produce a highly reactive compound ($^{\cdot}OH$) and sometimes they directly oxidize organic matter attached to the surface. Radicals reaction also occurs between the radicals and oxygen molecules [40]. Meanwhile, in reduction mechanism, electrons will be transferred to adsorbed oxygen and forms $\cdot O_2^-$ and in many cases; this transfer is also associated with reduction mechanism. Oxide-reduction equations [40-44]:

$h^+_{vb} + H_2O_{ads} \rightarrow {}^{\cdot}OH + H^+$ (Eq. 4)

$h^+_{vb} + OH^-_{ads} \rightarrow {}^{\cdot}OH$ (Eq. 5)

$e^-_{cb} + O_2 \rightarrow O_2^{-\bullet}$ (Eq. 6)

1.4 Physical characteristics of photocatalytic nanoparticles

The characteristics so that a nanomaterial can be called "photocatalytic nanomaterials" are outlined here. This subchapter is divided into three sections. Each section outlines the physical and photocatalytic properties of TiO_2, ZnO, stainless steel and Fe_2O_3 & Cr_2O_3 nanoparticles respectively.

1.4.1 TiO_2 nanoparticles

Two types of TiO_2 crystals are commonly known for their photocatalytic ability; rutile and anatase phases [35-50]. The bulk band gaps for rutile and anatase phases are 3.18 eV and 3.03 eV respectively. Both are abundant and stable phases of TiO_2. Anatase phase in particular has a maximum photon conversion efficiency of 6.8% when illuminated with light within 320 to 400 nm wavelength.

1.4.2 ZnO nanoparticles

Besides in nanoball form, ZnO nanoparticles in form of nanowires and nanoflowers are also present [61-64]. The most common and stable form of ZnO however is hexagonal wurtzite, with bulk band gap of 3.3 eV [51-59]. It has been reported that in terms of photocatalytic performance, it is less efficient than TiO_2. This is due to the difference in electron occupancy of the d-orbitals.

1.4.3 Stainless steel, Fe_2O_3 and Cr_2O_3 nanoparticles

Stainless steel was shown to become an active catalyst under certain conditions. 316 grade stainless steel reactor walls was reported to became an active catalyst under acidic conditions and elevated temperature [65].

They observed the deoxygenation of glycerol and levulinic acid when it is flowed into the reactor. The phenomenon was attributed to the synergistic effects between Fe, Ni and Cr that involved hydrogen spillover effects between sites that activate H_2(g) and sites responsible for hydrogenation steps. However, according to our findings, SUS316L nanoballs became an activated photocatalyst under UV-irradiation while being immersed in water (neutral environment) and at room temperature [3]. This indicates that the photoactivity of SUS316L is influenced by its size and also the synergistic effects of the Fe, Ni and Cr oxides.

One of the oxides present in SUS316L nanoballs are α-Fe_2O_3. It has strong visible light absorption, but it shows weak photoelectric/photocatalytic performance [68-72]. This is due to its short-lived carrier lifetimes caused by high density of defect or trap states. Other than α-Fe_2O_3, Cr_2O_3 nanoballs are also present within SUS316L nanoballs mixture. The effect of these metal oxides mixing together might enhance the photocatalytic ability of SUS316L nanoballs. The enhancement is caused by increased light absorption and ability to counteract the detrimental effect of electron-hole recombination.

Nanoballs can be classified as a zero-dimensional nanostructure; one-dimensional nanostructures include nanorods and nanowires, while two-dimensional nanostructures include thin films. It would be of great interest to have a simple method that can synthesize zero-dimensional nanostructures since the demand for nanostructures have been increasing [27].

1.5 Photocatalytic characteristics of nanoparticles: MB and PNDA as the indicator for photocatalytic activity

MB, a type of AZO dye, has been used commonly as an indicator of photocatalytic performance of photocatalytically active nanomaterials [60, 80-99]. The chemical structure of MB is shown in Figure 1-8. MB ($C_{16}H_{18}N_3SCl$, molecular weight is 319.9 g/mol) is thought to be toxic if swallowed. It is usually used as a dye in textile industry and as the reagent in 'blue bottle' experiments. The decomposition pathways of MB have been extensively documented. Identification of the intermediate products (by-products) that appear during decomposition is important, because it can help identify the decomposition pathway. Generally, photocatalytic materials act to oxidize the dye, while mineralization of carbon and hydrogen heteroatoms occurs. Apart from intermediate products such as Azure A, Azure B and phenol, decomposition of MB produces CO_2, NH_4^+, NO_3^- and SO_4^{2-} heteroatoms. The intermediate products can be detected using mass spectrometry, while the overall concentration of MB solution can be measured using photoabsorbance test.

Other than MB, methyl orange was considered as the dye for test of photocatalytic performance. However, it is very harmful since it is toxic even in small amounts. Besides that, other aqueous indicators such as phenol have been used to investigate the photodecomposition mechanism occurring in photocatalytic materials. However, since it is transparent, it would have been difficult to visually observe the rate of degradation during the photocatalytic activity test. Additionally, it would also be transparent to

photoabsorbance equipment. Therefore MB was chosen since it is far less toxic than methyl orange.

The wavelength of light which MB responds best for photodegradation is within 290nm to 340nm. UV light with λ= 354nm was used because it is nearest to the optimal response of MB. Also, TiO_2 and ZnO photocatalysts respond optimally to UV-light in the mentioned wavelength [23-24, 27, 43].

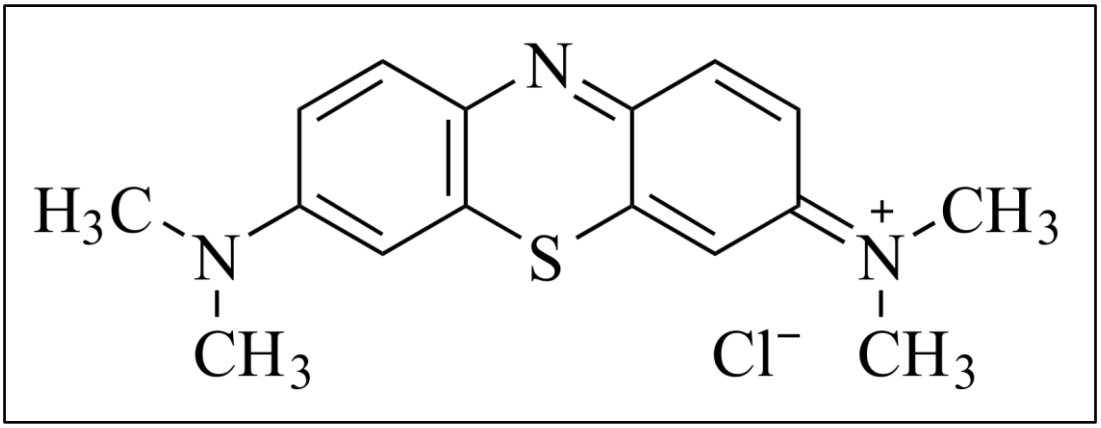

Figure 1-8 MB chemical structure.

P-nitrosodimethylaniline (PNDA) is used as the hydroxyl radicals (·OH) indicator [73-79]. It is a type of hydroxyl radicals scavenger. This means that it only reacts with hydroxyl radical where it becomes decomposed by the oxidative nature of hydroxyl radicals. Figure 1-9 shows the chemical structure of PNDA. ·OH radicals are generated during photocatalytic reaction. It contributes to the reaction by decomposing the organic pollutants in water. Measuring the amount of ·OH radicals generated by each type of nanoballs is important because it can indicate the photocatalytic performance of the nanoballs. Therefore, to investigate the

amount of ·OH radicals generated by the nanoballs, the photobleaching of PNDA was measured [73,77].

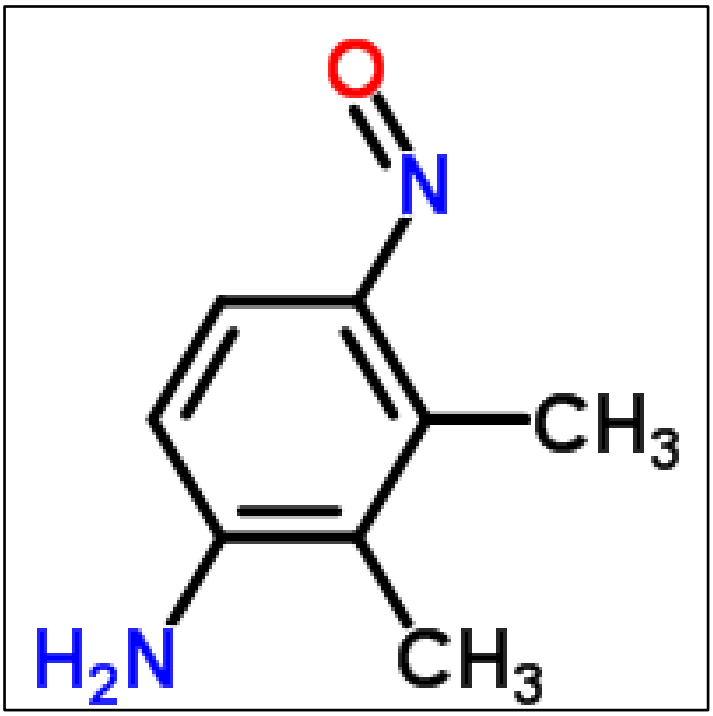

Figure 1-9 Chemical structure of PNDA.

1.6 Aims of thesis

This research aims to synthesize oxide nanoballs that are photocatalytically active. Three types of materials were selected due to ease of comparison and potential discovery of new photocatalytic material. Ti and Zn were selected because of their excellent photocatalytic ability in nanostructure form.

Submerged glow-discharge plasma is the only method that is viable for synthesis of SUS316L nanoballs [3]. Previously, the smallest stainless steel nanoballs were only around 20nm in size. Our method was able to produce SUS316L nanoballs with sizes less than 10nm. Besides that, it is cost-effective and can easily synthesize other kinds of multialloy compounds such as bimetallic compounds.

SUS316L (stainless steel) was selected as the new candidate for photocatalytic material because of the semiconducting ability of its passivation layer. Furthermore, Fe_2O_3 and Cr_2O_3 were shown to have photocatalytic activity.

It is also a material that is commonly used in industries because it is economical, tough, and corrosion-resistant. The steel industry could benefit from the synthesis of stainless steel nanoparticles. An additional usage for stainless steel is beneficial for the steel industry to add value to their scrap material and to increase the reusability of steel products in general. Therefore, stainless steel nanoparticles could revitalize the steel industry.

1.7 Outline of thesis

Chapter 1 is the introduction of this thesis. It outlines the usage of plasma processing as a method of nanoparticles production and the background of photocatalytic nanoparticles.

Chapter 2 is the explanation regarding experimental setup and characterization methods. The experiments are divided into three major steps; synthesis of nanoballs, characterization of nanoballs and characterization of photocatalytic performance of the nanoballs.

Chapter 3 is the results of characterization of the physical properties of nanoballs. SEM, TEM, XRD and BET were used to conduct the investigation of the physical properties of the nanoballs.

Chapter 4 is the results of the photocatalytic properties of nanoballs. MB and PNDA was used to characterize the photocatalytic performance of the nanoballs. The mechanism of MB photodecomposition is also discussed in this chapter.

Chapter 5 is the general conclusion. It summarizes this thesis and the experimental results. The recommendations for future research and prospects are also outlined in this chapter.

References

[1] A. R. Denaro, A. Hickling, Journal of the Electrochemical Society, **105** (1958) 265-270.

[2] G. Saito, S. Hosokai, T. Akiyama, S. Yoshida, S. Yatsu, and S. Watanabe, Journal of the Physical Society of Japan, **79** (2010) 083501-1-3.

[3] M. R. M. bin Julaihi, S. Yatsu, M. Jeem, S. Watanabe, Journal of Experimental Nanoscience, (2014) DOI: 10.1080/17458080.2014.951408, 1-18 .

[4] T. A. Kareem, A. A. Kaliani, Ionics, **18** (2011) 315–327.

[5] J. P. Chang, J. W. Coburn, Journal of Vacuum Science and Technology, **A21** (2003) S145-S151.

[6] Y. Toriyabe, undergraduate thesis (2007)

[7] Y. Toriyabe, S. Watanabe, S. Yatsu, T. Shibayama, T. Mizuno, Applied Physics Letters, **91** (2007) 041501.

[8] N. Parkansky, G. Frenkel, B. Alterkop, I. Beilis, R.L. Boxman, Z. Barkay, Yu. Rosenberg, Journal of Alloys and Compounds, **464** (2007) 483-487.

[9] W. M. Qiao, Y. Song, S. Y. Lim, S.H. Hong, S. H. Yoon, I. Mochida, T. Imaoka, Letters to the Editor/Carbon, **44** (2006) 187-193.

[10] Y. Q. Zhu, H. W. Kroto, D. R. M. Walton, H. Lange, A. Huczko, Chemical Physics Letters, **365** (2002) 457-463.

[11] S.Y. Moon, J. W. Han, W. Choe, Thin Solid Films, **506-507** (2006) 355-359.

[12] K.T. Rie, A. Gebauer, J. Wohle, Surface & Coatings Technology, **86-87** (1996) 498-506.

[13] F. E. Kruis, H. Fissan, A. Peled, Journal of Aerosol Science, **29** (1998) 511-535.

[14] A. Bogaerts, E. Neyts, R. Gijbels, J. van der Mullen, Spectrochimica Acta Part B, **57** (2002) 609-658.

[15] H. Hahn, Nanostructured Materials, **9** (1997) 3-12.

[16] M. Omrani, M. Habibi, R. Amrollahi, A. Khosravi, International Journal of Hydrogen Energy, **37** (2012) 14676-14686.

[17] H. Lee, S. H. Park, S. J. Kim, Y. K. Park, B. H. Kim, S. C. Jung, Microelectronic Engineering, **126** (2014) 153-157.

[18] Q. Chen, T. Kaneko, R. Hatakeyama, Current Applied Physics, **11** (2011) S63-S66.

[19] N. S. von Brisinski, O. Hofft, F. Endres, Journal of Molecular Liquids, **192** (2014) 59-66.
[20] Y. Hattori, S. Nomura, S. Mukasa, H. Toyota, T. Inoue, T. Kasahara, Journal of Alloys and Compounds, **560** (2013) 105-110.
[21] Y. Hattori, S. Nomura, S. Mukasa, H. Toyota, T. Inoue, T. Usui, Journal of Alloys and Compounds, **578** (2013) 148-152.
[22] Y. Cheng, M. Shigeta, S. Choi, T. Watanabe, Chemical Engineering Journal, **183** (2012) 483-491.
[23] A. Fujishima, T. N. Rao, D. A. Tyrk, Journal of Photochemistry and Photobiology C: Photochemistry Reviews, **1** (2000) 1-21.
[24] J. Z. Zhang, MRS Bulletin, **36** (2011) 48-54.
[25] L. Zhang, T. Kanki, N. Sano, A. Toyoda, Separation and Purification Technology, **31** (2003) 105-110.
[26] F. Chen, Y. Xie, J. Zhao, G. Lu, Chemosphere, **44** (2001) 1159-1168.
[27] D. Barreca, G. Carraro, V. Gombac, A. Gasparotto, C. Maccato, P. Fornasiero, E. Tondello, Advanced Functional Materials, **21** (2011) 2611-2623.
[28] S. K. Kansal, A. H. Ali, S. Kapoor, D. W. Bahnemann, Separation and Purification Technology, **80** (2011) 125-130.
[29] X. He, F. Wu, M. Zheng, Diamond and Related Materials, **16** (2007) 311-315.
[30] S. Rengaraj, X. Z. Li, Journal of Molecular Catalysis A: Chemical, **243** (2006) 60-67.
[31] Y. Zhao, J.M. Hong, J.J. Zhu, Journal of Crystal Growth, **270** (2004) 438-445.
[32] G. Saito, S. Hosokai, M. Tsubota, T. Akiyama, Journal of Applied Physics, **110** (2011) 023302.
[33] Z. Jiang, X. Yu, Y. Shi, Y. Meng, Thin Solid Films, **518** (2010) 6609-6613.
[34] K. Watanabe, D. Menzel, N. Nilius, H.-J. Freund, Chemical Reviews, **106** (2006) 4301-4321.
[35] A. Fujishima, K. Hashimoto, T. Watanabe, TiO_2 photocatalysis: fundamentals and applications, (1997) Trans. BKC Inc: Japan, BKC Inc.
[36] P. Cheng, C. Deng, M. Gu, W. Shangguan, Journal of Materials Science, **42** (2007) 9239–9244
[37] J. Ye, J. Tang, NIMS Now, **1** (2003) 1-8.

[38] M. Ni, M. K. H. Leung, D. Y. C. Leung, K. Sumathy, Renewable and Sustainable Energy Reviews, **11** (2005) 401-425.
[39] J. –M. Hermann, C. Guillard, P. Pichat, Catalysis Today, **17** (1993) 7-20.
[40] F. E. Osterloh, B. A. Parkinson, MRS Bulletin, **36** (2011) 17-22.
[41] A. Kudo, MRS Bulletin, **36** (2011) 32-38.
[42] G. K. Mor, K. Shankar, M. Paulose, O. K. Varghese, C. A. Grimes, Nano Letters, **5** (2005) 191-195.
[43] H. Atwater, MRS Bulletin, **36** (2011) 57-62.
[44] T. Yoshimura, K. Takeda, H. Sasaki, M. Tatsui, Applied Surface Science, **256** (2009) 112-115
[45] P. A. Pekakis, N. P. Xekoukoulotakis, D. Mantzavinos, Water Research, **40** (2006) 1276-1286.
[46] P. S. S. Kumar, M. R. Raj, S. Anandan, Solar Energy Materials and Solar Cells, **94** (2010) 1783-1789.
[47] A. Paleologou, H. Marakas, N. P. Xekoukoulotakis, A. Moya, Y. Vergara, N. Kalogerakis, P. Gikas, D. Mantzavinos, Catalysis Today, **129** (2007) 136-142.
[48] K. J. Shieh et. al., Nanomed. Nanotech. Bio. Med., 2 (2006) 121-126.
[49] H. Gnaser, A. Orendorz, C. Ziegler, E. Rowlett, W. Bock, Solar Energy Materials and Solar Cells, **252** (2006) 6996-6999.
[50] J. W. Choi, S. E. Lee, B. G. Lee, Y. S. Jeong, H. J. Oh, C. S. Chi, Transactions of Nonferrous Metals Society of China, **19** (2009) 1027-1030.
[51] G. Saito, S. Hosokai, T. Akiyama, Materials Chemistry and Physics, **130** (2011) 79-83.
[52]http://www.thunderbolts.info/eg_draft/images/plasma_discharges_diagram_802x557.jpg, retrieved 2014/03/01.
[53] A. Lei, B. Qu, W. Zhou, Y. Wang, Q. Zhang, Bingsuo Zou, Materials Letters, 66 (2011) 72-75.
[54] S. Saremi-Yarahmadi, A. A. Tahir, B. Vaidyanathan, K. G. U. Wijayantha, Materials Letters, **63** (2009) 523-526.
[55] S.C. Kwon, M. Fana, T.D. Wheelock, B. Saha, Separation and Purification Technology, **58** (2007) 40–48.
[56] A. A. Tahir, K. G. U. Wijayantha, S. Saremi-Yarahmadi, M. Mazhar, V. McKee, Chemistry of Materials, **21** (2009) 3763–3772.
[57] V. R. Satsangi, S. Kumari, A. P. Singh, R. Shrivastav, S. Dass,

International Journal of Hydrogen Energy, **33** (2008) 312 – 318.
[58] S. Boumaza, A. Boudjemaa, S. Omeiri, R. Bouarab, A. Bouguelia, M. Trari, Solar Energy, **84** (2010) 715–721.
[59] M.A. Gondal, A. Hameed, Z. H. Yamani, A. Suwaiyan, Applied Catalysis A: General, **268** (2004) 159–167.
[60] A. Houas, H. Laccheb, M. Ksibi, E. Elaloui, C. Guillard, J-M. Herrmann, Applied Catalysis B: Environmental, **31** (2001) 145-157.
[61] T. J. LaTempa, X. Feng, M. Paulose, C. A. Grimes, Journal of Physical Chemistry C, **113** (2009) 16293–16298.
[62] N. J. Cherepy, D. B. Liston, J. A. Lovejoy, H. Deng, J. Z. Zhang, Journal of Physical Chemistry B, **102** (1998) 770-776.
[63] M.I. Dominguez, M. Sanchez, M.A. Centeno, M. Montes, J.A. Odriozola, Journal of Molecular Catalysis A: Chemical, 277 (2007) 145–154.
[64] M.I. Dominguez, M. Sanchez, M.A. Centeno, M. Montes, J.A. Odriozola, Applied Catalysis A: General, **302** (2006) 96–103.
[65] D. Di Mondo, D. Ashok, F. Waldie, N. Schrier, M. Morrison, M. Schlaf, ACS Catalysis, **1** (2011) 355-364.
[66] M. Uzunova, M. Kostadinov, J. Georgieva, C. Dushkin, D. Todorovsky, N. Philippidis, I. Poulios, S. Sotiropoulos, Applied Catalysis B: Environmental, **73** (2007) 23-33.
[67] Y. Chen, D. Dionysiou, Applied Catalysis B: Environmental, **62** (2006) 255-264.
[68] T. K. Townsend, E. M. Sabio, N. D. Browning, F. E. Osterloh, Energy & Environmental Science, **4** (2011) 4270-4275.
[69] L. -S. Zhong, J. -S.Hu, H. -P. Liang, A. –M. Cao, W. –G. Song, L. –J. Wan, Advanced Materials, **18** (2006) 2426-2432.
[70] J. Ding, Q. Zhong, S. Zhang, Journal of Molecular Catalysis A: Chemical, **393** (2014) 222-231.
[71] A. Hakuli, M. E. Harlin, L. B. Backman, A. O. I. Krause, Journal of Catalysis, **184** (1999) 349-356.
[72] G. Guan, T. Kida, A. Yoshida, Applied Catalysis B: Environmental, **41** (2003) 387-396.
[73] J. H. Baxendale, A. A. Khan, International Journal for Radiation Physics and Chemistry, **1** (1969) 11-24.
[74] S. Hisaindee, M. A. Meetani, M. A. Rauf, Trends in Analytical

Chemistry, **49** (2013) 31-44.
[75] B. G. Kwon, S. Ryu, J. Yoon, Journal of Industrial Engineering Chemistry, **15** (2009) 809-812.
[76] L. Zang, P. Qu, J. Zhao, T. Shen, H. Hidaka, Journal of Molecular Catalysis A: Chemical, **120** (1997) 235-245.
[77] S. S. Shinde, C. H. Bhosale, K. Y. Rajpure, J. H. Lee, Journal of Photochemistry and Photobiology B: Biology, (2014) http://dx.doi.org/10.1016/j.jphotobiol.2014.10.015, 1-18.
[78] M. E. Simonsen, J. Muff, L. R. Bennedsen, K. P. Kowalski, E. G. Sogaard, Journal of Photochemistry and Photobiology A: Chemistry, **216** (2010) 244-249.
[79] B. Tryba, M.Toyoda, A. W. Morawski, R. Nonaka, M. Inagaki, Applied Catalysis B: Environmental, **71** (2007) 163-168.
[80] A. I. Kozlov, A. P. Kozlova, H. Liu, Y. Iwasawa, Applied Catalysis A: General, **182** (1999) 9-28.
[81] K. J. Kim, H. G. Ahn, Applied Catalysis B: Environmental, **91** (2009) 308-318.
[82] K. Qian, J. Fang, W. Huang, B. He, Z. Jiang, Y. Ma, S. Wei, Journal of Molecular Catalysis A: Chemical, **320** (2010) 97-105.
[83] E. Kusiak-Nejman, M. Janus, B. Grzmil, A. W. Morawksi, Journal of Photochemistry and Photobiology A: Chemistry, **226** (2011) 68-72.
[84] E. E. Oguzie, G. N. Onuoha, A. I. Onuchukwu, Materials Chemistry and Physics, **89** (2005) 305-311.
[85] Z.D. Wei, F. Yin, L.L. Li, X.W. Wei, X.A. Liu, Journal of Electroanalytical Chemistry, **541** (2003) 185-191.
[86] S. Takenaka, A. Hirata, E. Tanabe, H. Matsune, M. Kishida, Journal of Catalysis, **274** (2010) 228–238.
[87] L. V. Mattos, F. B. Noronha, Journal of Power Sources, **145** (2005) 10-15.
[88] K. Imamura, E. Ikeda, T. Nagayasu, T. Sakiyama, K. Nakanishi, Journal of Colloid and Interface Science, **245** (2002) 50-57.
[89] C. Yogi, K. Kojjima, N. Wada, H. Tokumoto, T. Takai, T. Mizoguchi, H. Tamiaki, Thin Solid Films, **516** (2008) 5881-5884.
[90] R. Solarska, B.D. Alexander, A. Braun, R. Jurczakowski, G. Fortunato, M. Stiefel, T. Graule, J. Augustynski, Electrochimica Acta, **55** (2010) 7780-7787.

[91] A. Houas, H. Laccheb, M. Ksibi, E. Elaloui, C. Guillard, J-M. Herrmann, Applied Catalysis B: Environmental, **31** (2001) 145-157.
[92] K. L. Arvan, G. A Korsunovskii, Zhurnal Prikladnoi Spektroskopii, **4** (1971) 722-724.
[93] C. Noubactep, Journal of Hazardous Materials, **166** (2009) 79-87.
[94] C. H. Kwon, H. Shin, J. H. Kim, W. S. Choi, K. H. Yoon, Materials Chemistry and Physics, **86** (2004) 78-82.
[95] C. Liu, X. Tang, C. Mo, Z. Qiang, Journal of Solid State Chemistry, **181** (2008) 913-919.
[96] K. J. Hwang, J. W. Lee, W. G. Shim, H. D. Jang, S. I. Lee, S. J. Yoo, Advanced Powder Technology, **23** (2012) 414-418..
[97] S. Lakshmi, R. Reganathan, S. Fujita, Journal of Photochemistry and Photobiology A: Chemistry, **88** (1995), 163-167.
[98] N. Liu, G. Sun, Dyes and Pigments, **91** (2011) 215-224.
[99] S. Horikiri, N. Teshima, Y. Saruki, H. Nishikawa, T. Sakai, Bunseki Kagaku, **52** (2003) 881-885.

Chapter 2 Experimental Procedure and Characterization Methods

Chapter 2 Experimental procedure and characterization methods

2.1 Submerged glow-discharge plasma and photocatalysis test

2.1.1 Submerged glow-discharge plasma setup

Figure 2-1 shows the setup for nanoballs synthesis. A platinum wire of 1000mm in length and 0.5mm in diameter was used as the anode. This wire was shaped to conform to the contours of the glass frame holder measuring 45mm in height and 60mm in width. A stainless steel (SUS316L) wire measuring 150mm in length and 1.0mm in diameter with purity of 99.99% mass (Nilaco, Tokyo, Japan) was used as the cathode. This wire was inserted into a glass tube to obtain an exposed length of 20mm; the exposed part functioned as the net actual electrode. The glass tube functions as an insulation to provide the exposed length mentioned before. The electrolyte was a 300ml solution of 0.1 mol K_2CO_3 with 99.5% purity. The submerged glow-discharge experiment was repeated by replacing the SUS316L wire with zinc (99.1% purity, Nilaco, Tokyo, Japan) and titanium (99.5% purity, Nilaco, Tokyo, Japan) wire. The dimensions of the zinc and titanium wires were identical to the dimensions of SUS316L wire.

2.1.2 Photocatalysis test setup

Figure 2-2 shows the schematic diagram of the experimental setup used during photocatalysis test. The MB/PNDA mixture was irradiated with UV-light for a predetermined time period during the photocatalysis test.

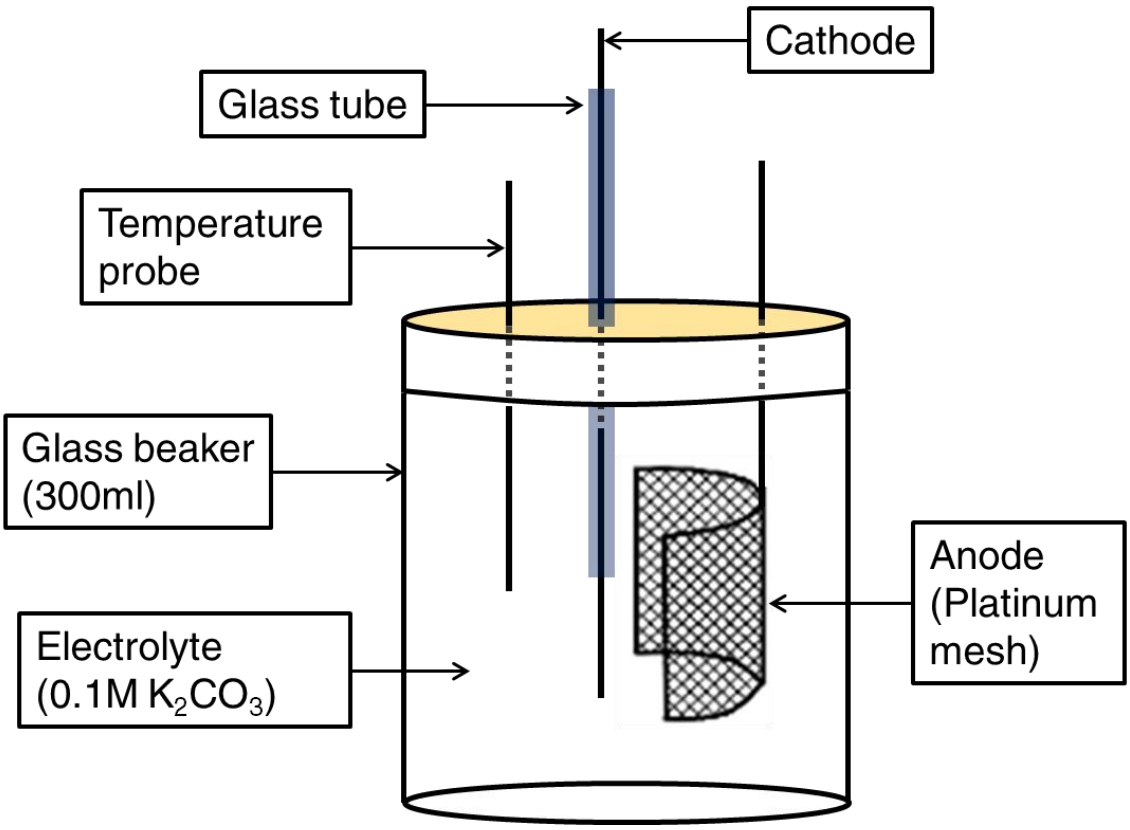

Figure 2-1 Schematic diagram of experimental setup for submerged glow-discharge plasma.

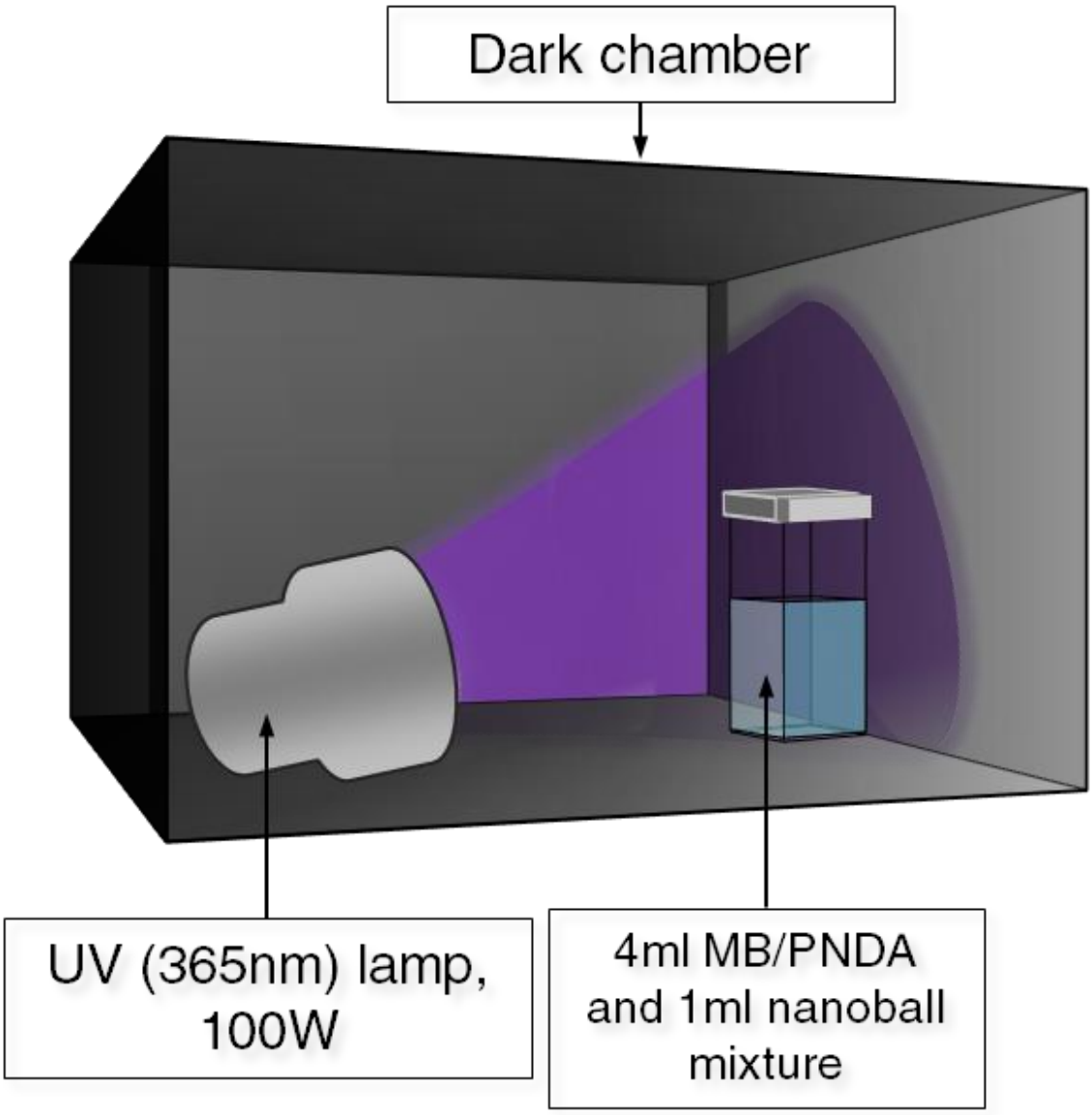

Figure 2-2 Schematic diagram of experimental setup for photocatalysis test.

2.2 Characterizing the physical properties of nanoballs

The nanoballs were synthesized via submerged glow-discharge plasma process. The anode and cathode were dipped in solution of sulphuric acid (0.01 mol concentration) for a few seconds and then washed with purified water. The electrolyte was warmed until it reached at least 80°Celcius, then voltage was applied until plasma forms under constant-voltage control (Figure 2-3 and Figure 2-4). Then the voltage was fixed at a constant value for 3 hours. The sustained voltages for each type of electrode were 95V for Zn, 120V for Ti and 130V for SUS316L. After glow-discharge, the products existing in the electrolyte were collected via centrifuging (Figure 2-5) and washing with purified water to remove traces of remaining electrolyte.

Table 1 Glow-discharge voltages for present nanoballs synthesis.

Nanoball type	**Glow-discharge voltage (V)**
ZnO	95
TiO_2	120
SUS	130

Figure 2-3 Takasago GP0250-10R regulated DC power supply.

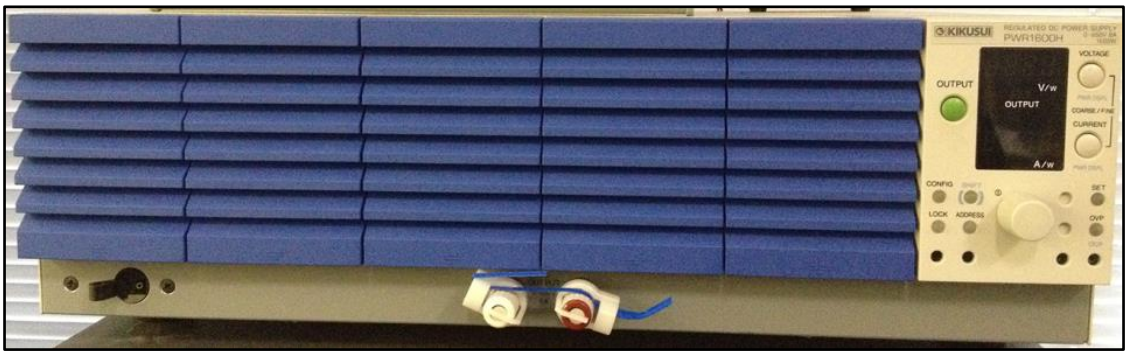

Figure 2-4 Kikusui PWR1600H regulated DC power supply.

Figure 2-5 Tomy LC-200 centrifuge.

2.2.1 Scanning electron microscopy (SEM)

FE-SEM images of the nanoballs were taken using a JSM7001FA (JEOL, Tokyo, Japan) FE-SEM at an operating voltage of 15kV, shown in Figure 2-6. The aqueous solution containing the nanoballs was deposited onto a metallic plate for SEM observation. For TiO_2 and ZnO nanoballs were deposited onto a stainless steel plate while SUS316L nanoballs were deposited onto a zinc plate for SEM observation.

2.2.2 Transmission electron microscopy (TEM)

TEM images were taken using an H-700V (Hitachi High-Technologies, Japan) and Titan3 G2 60-300 S/TEM (FEI, Oregon, USA) TEM at an operating voltage of 150kV and 300kV respectively. The aqueous solution containing the nanoballs was deposited onto a Quantifoil grid for TEM observation.

2.2.3 X-ray diffraction (XRD)

XRD observation was carried out using a Miniflex II (Rigaku, Tokyo, Japan) diffractometer. XRD profiles for the nanoballs were recorded using Cu $K\alpha_1$ (λ = 1.54056Å) in the range 10-90° (2θ). The oxide compounds and crystal structures of the nanoballs can be investigated using XRD.

2.2.4 Nanoball yield evaluation

The amount of nanoballs collected was estimated by measuring the mass of the cathode before and after submerged glow-discharge plasma experiment.

2.2.5 Brunauer-Emmett-Teller (BET) test

BET test was conducted using Autosorb 6 analyzer (Quantachrome Instruments, Florida, USA) by volumetric method. The purpose was to measure the nanoballs' surface area and total pore volume. The nanoballs were freeze-dried using an EYELA FP-2100 freeze dryer for 12 hours to convert the nanoballs into powder form. Then the powders were degassed with nitrogen for 4 hours at 200°C before taking measurements using BET.

2.3 Evaluation of photocatalytic activity of nanoballs

The photocatalytic activity of the nanoballs was determined by the photodecomposition of MB. An aqueous solution of MB (4ml) and nanoballs (1ml) in a 5ml plastic cell was exposed to UV irradiation for 24 hours. The initial concentration of MB was 0.1g/1000ml. The UV light used was a UVP Blak-Ray B100AP lamp having 100W power and emitting UV light at 354nm wavelength. During the duration of UV-irradiation, the setup was contained inside a dark chamber to eliminate the influence of external light sources such as fluorescent lamps and sunlight.

The images of MB dyes contained in PMMA cuvettes during photocatalytic test were taken at specified time intervals. The purpose was to visually inspect the photodecomposition of MB in presence of synthesized nanoballs and in UV light.

2.3.1 Photoabsorbance test

UV/VIS spectrophotometer (Jasco V-630, Maryland, USA) was used to measure the relative concentration of MB before and after the photocatalysis test. The equipment is shown in Figure 2-7. Before the photoabsorbance test, the UV-irradiated MB and nanoballs mixture were centrifuged to separate the MB solution from the nanoballs. By measuring the light absorbance of the dye solution, the transparency of the MB solution after photocatalyis experiment can be measured.

2.3.2 Evaluation of photodecomposition rate and constants

To measure the photocatalytic performance of the nanoballs, the photodecomposition constants are calculated. The formula to calculate photodecomposition constant (μ) is;

$$\mathrm{I(t)} = I_0 e^{-\mu t}$$

where I(t) is the intensity at a given time, I_o is the initial concentration, μ is the photodecomposition constant and t is time.

2.3.3 Mass spectrometry

Mass spectrometry was used to determine the chemical compounds that were present after the photocatalysis test. It is important to determine the kind of chemical compounds present because they can show the difference in the photocatalytic reaction that occurs in the nanoballs under UV-light irradiation.

Figure 2-6 JEOL JSM7001FA FE-SEM.

Figure 2-7 JASCO V-630 UV-Vis spectrophotometer.

References

[1] J. H. Baxendale, A. A. Khan, International Journal for Radiation Physics and Chemistry, **1** (1969) 11-24.
[2] S. Hisaindee, M. A. Meetani, M. A. Rauf, Trends in Analytical Chemistry, **49** (2013) 31-44.
[3] B. G. Kwon, S. Ryu, J. Yoon, Journal of Industrial Engineering Chemistry, **15** (2009) 809-812.
[4] L. Zang, P. Qu, J. Zhao, T. Shen, H. Hidaka, Journal of Molecular Catalysis A: Chemical, **120** (1997) 235-245.
[5] C. Liu, X. Tang, C. Mo, Z. Qiang, Journal of Solid State Chemistry, **181** (2008) 913-919.
[6] M. E. Simonsen, J. Muff, L. R. Bennedsen, K. P. Kowalski, E. G. Sogaard, Journal of Photochemistry and Photobiology A: Chemistry, **216** (2010) 244-249.
[7] B. Tryba, M.Toyoda, A. W. Morawski, R. Nonaka, M. Inagaki, Applied Catalysis B: Environmental, **71** (2007) 163-168.
[8] A. I. Kozlov, A. P. Kozlova, H. Liu, Y. Iwasawa, Applied Catalysis A: General, **182** (1999) 9-28.
[9] K. J. Kim, H. G. Ahn, Applied Catalysis B: Environmental, **91** (2009) 308-318.
[10] K. Qian, J. Fang, W. Huang, B. He, Z. Jiang, Y. Ma, S. Wei, Journal of Molecular Catalysis A: Chemical, **320** (2010) 97-105.
[11] C. Noubactep, Journal of Hazardous Materials, **166** (2009) 79-87.
[12] E. E. Oguzie, G. N. Onuoha, A. I. Onuchukwu, Materials Chemistry and Physics, **89** (2005) 305-311.
[13] Z.D. Wei, F. Yin, L.L. Li, X.W. Wei, X.A. Liu, Journal of Electroanalytical Chemistry, **541** (2003) 185-191.
[14] K. L. Arvan, G. A Korsunovskii, Zhurnal Prikladnoi Spektroskopii, **4** (1971) 722-724.
[15] L. V. Mattos, F. B. Noronha, Journal of Power Sources, **145** (2005) 10-15.
[16] K. J. Hwang, J. W. Lee, W. G. Shim, H. D. Jang, S. I. Lee, S. J. Yoo, Advanced Powder Technology, **23** (2012) 414-418...
[17] C. Yogi, K. Kojjima, N. Wada, H. Tokumoto, T. Takai, T. Mizoguchi, H. Tamiaki, Thin Solid Films, **516** (2008) 5881-5884.
[18] R. Solarska, B.D. Alexander, A. Braun, R. Jurczakowski, G. Fortunato,

M. Stiefel, T. Graule, J. Augustynski, Electrochimica Acta, **55** (2010) 7780-7787.
[19] A. Houas, H. Laccheb, M. Ksibi, E. Elaloui, C. Guillard, J-M. Herrmann, Applied Catalysis B: Environmental, **31** (2001) 145-157.
[20] S. Lakshmi, R. Reganathan, S. Fujita, Journal of Photochemistry and Photobiology A: Chemistry, **88** (1995), 163-167.

Chapter 3 Experimental Results and Discussion: Physical Characteristics of Nanoballs

Chapter 3 Experimental results and discussions: Physical characteristics of nanoballs

3.1 Scanning electron microscopy (SEM) results

Figure 3-1 shows the SEM images of the nanoballs at 20,000 times magnification after glow-discharge plasma synthesis and centrifuging to remove K_2CO_3 electrolyte. From left to right are SUS 316L, ZnO and TiO_2 respectively. In all three images, the nanoballs have uniformly spherical shape and are nanosized. It can be seen that the nanoballs size falls within a range of 100nm to 1μm.

Figure 3-2 shows the SEM-EDS spectra for SUS316L wire and nanoballs. There is an increase in oxygen content for the synthesized nanoball compared to pure SUS316L wire.

Figure 3-3 shows the SEM-EDS results of the wires used as the cathodes for nanoballs synthesis. Apart from pure metallic elements, there is very little oxide species on the surface of the wires. This shows that the wires were composed of nearly pure metallic materials.

Figure 3-4 shows the SEM-EDS results of the nanoballs, while Tables 3-5 show the elemental composition of the nanoballs and their parent materials. In Figure 3-4(a), O atoms were detected alongside Fe, Mn, Ni and Cr atoms on the surface of the nanoballs. Table 3 shows the elemental composition of SUS316L wire before submerged glow discharge plasma, and the elemental composition of the nanoballs after submerged glow discharge plasma. Before the application of plasma, SUS316L wire consisted of Fe, Ni and Cr atoms, which is consistent with the elemental

composition of SUS316L. After the application of plasma, the nanoballs were found to contain O atoms, in addition to Fe, Ni and Cr atoms of its parent material. These results indicate that the surfaces of the nanoballs were in their oxidized form after synthesis. In Figure 3-4(b), O atoms were detected in addition to Zn atoms on the surface of ZnO nanoballs. Table 5 shows the elemental composition of Zn wire and ZnO nanoballs. It is apparent that the amount of O has increased considerably in the case of ZnO nanoballs compared to its parent material.

In Figure 3-4(c), O atoms were detected in addition to Ti atoms on the surface of TiO_2 nanoballs. Table 4 shows the elemental composition of Ti wire and TiO_2 nanoballs. Similar to the case of SUS316L and ZnO nanoballs, after submerged glow discharge, TiO_2 nanoballs were found to contain an increased amount of O atoms compared to Ti wire.

Generally, for all three types of nanoballs, an oxide layer is thought to be present on the surfaces of the nanoballs. The oxide layer is evenly distributed on their surfaces. This oxide layer has an important role in photocatalysis, since they are reactive towards UV light, releasing ·OH free radicals. Since the oxide layer on the nanoballs has been identified, further investigation of the cross-sections of the nanoballs is needed. Also, the microstructure between the oxide surface and the nanoball bulk volume is of interest, to determine the growth mechanism of the oxide surface.

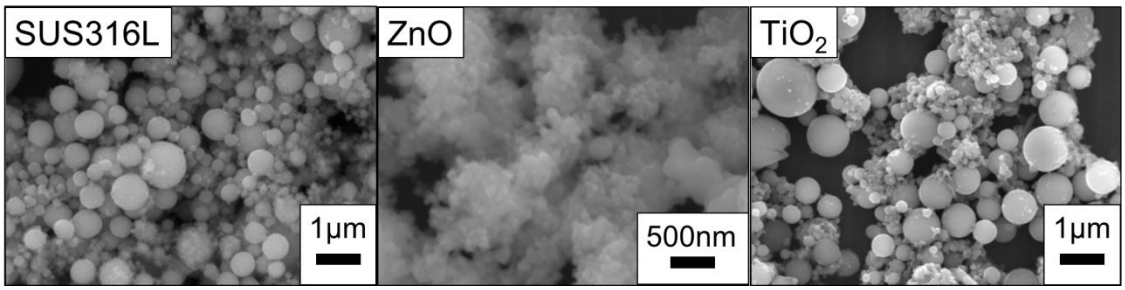

Figure 3-1 SEM images of nanoballs.

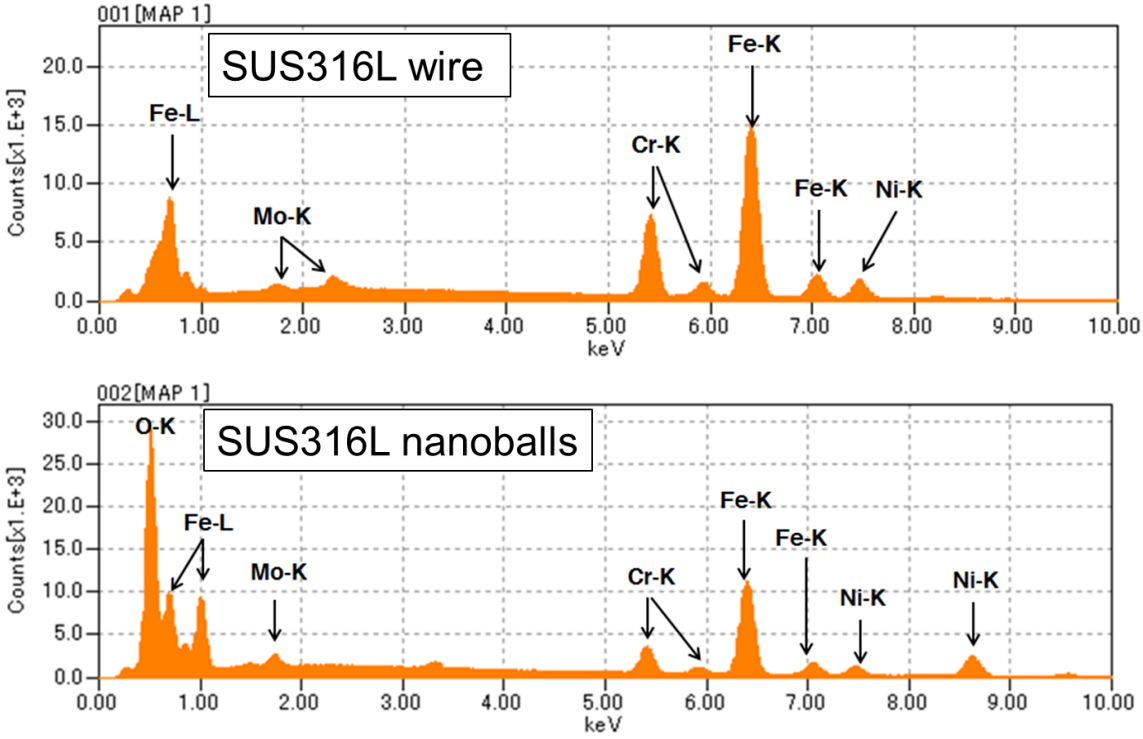

Figure 3-2 SEM-EDS spectrum of SUS316L wire and SUS316L nanoballs.

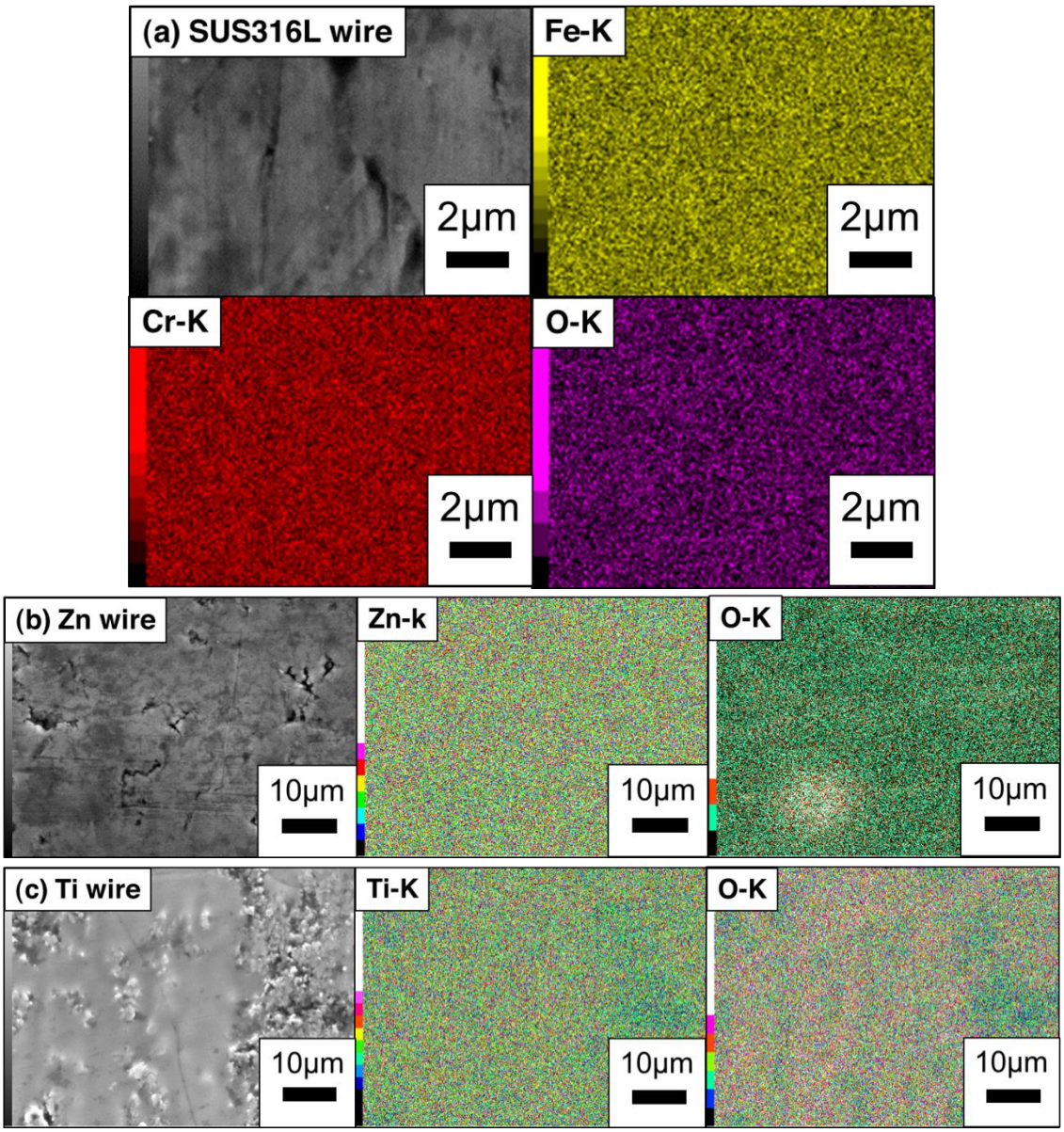

Figure 3-3 (a) SEM-EDS map of SUS316L wire showing Fe-K, Cr-K, and Ni-K. (b) SEM-EDS map of Zn wire showing Zn-K and O-K. (c) SEM-EDS map of Ti wire showing Ti-K and O-K.

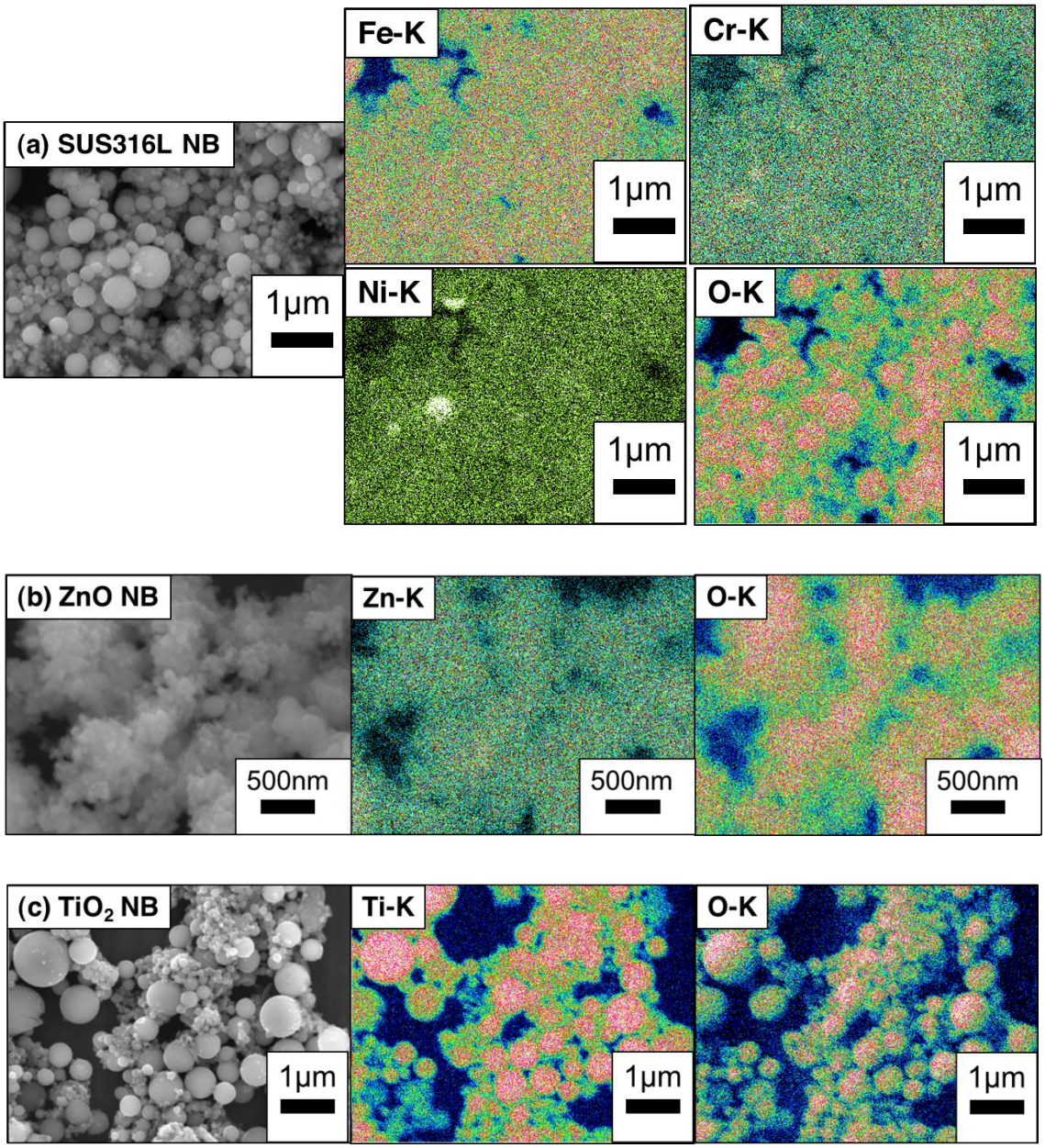

Figure 3-4 (a) SEM-EDS map of SUS316L nanoballs showing Fe-K, Cr-K, Ni-K and O-K. (b) SEM-EDS map of ZnO nanoballs showing Zn-K and O-K. (c) SEM-EDS map of TiO_2 nanoballs showing Ti-K and O-K.

The tables below show the elemental compositions of the wires and nanoballs.

Table 2 Elemental composition of SUS316L wire and SUS316L nanoballs.

Element	**Mole percent (%)**	
	SUS316L wire	SUS316L nanoballs
Fe	68.39	43.07
Cr	19.30	8.17
Ni	12.30	6.89
O	0	41.87
Total	100.00	100.00

Table 3 Elemental composition of Zn wire and ZnO nanoballs.

Element	**Mole percent (%)**	
	Zn wire	ZnO nanoballs
Zn	98.37	44.93
O	1.63	55.07
Total	100.00	100.00
Total	100.00	100.00

Table 4 Elemental composition of Ti wire and TiO_2 nanoballs.

Element	**Mole percent (%)**	
	Ti wire	TiO_2 nanoballs
Ti	92.32	33.35
O	7.68	66.65

3.2 Transmission electron microscopy (TEM) results

Figure 3-5 shows the TEM images of the nanoballs after glow-discharge plasma synthesis and centrifuging to remove K_2CO_3 electrolyte. From left to right are SUS316L, ZnO and TiO_2, respectively. In all three images, the nanoballs have uniformly spherical shape and are nanosized. It can be seen that the nanoballs' size falls within a range of 50-400 nm, as confirmed by the particle size distribution and BET method. In terms of particle size uniformity, the size of ZnO nanoballs fell within a narrow range of 60-150 nm. In the case of SUS316L and TiO_2 nanoballs, their sizes fell within a wider range than those of ZnO nanoballs. For SUS316L nanoballs, their sizes fell between 30 and 300 nm, while for TiO_2 nanoballs their sizes fell between 30 and 400 nm**.**

Figure 3-6 shows the high-resolution transmission electron microscope (HRTEM) image of a SUS316L nanoball measuring roughly 40nm in diameter. The spinel structure can be seen in the figure above, particularly in the center of the nanoball. The lattice constant was measured to be 1.6 angstrom. The measurement corresponds to the [110] plane of spinel structure. This spinel stainless steel structure was observed in SUS316L nanoballs with sizes less than 50nm.

Figure 3-7 shows the TEM-EDS image of SUS316L nanoballs. Depending on the size of the nanoball, the elemental composition is different. For example, nanoballs more than 200nm in diameter are composed of mainly Fe. For nanoballs below 200nm, Cr and Ni are the dominant elements. There was also evidence of nanoballs that are composed of multiple elements (multicomponent). This can be observed in Figure 3-7 where Fe, Cr, Ni and O existed in a single nanoball. Additionally, O can be found throughout the surfaces of the nanoballs regardless of their size. This means that nearly all of the SUS316L nanoballs were in their oxidized state.

HRTEM reveals the lattice parameter to be 0.16nm and the crystal structure is spinel. TEM-EDS confirmed the presence of metallic oxide species such as iron oxide, chromium oxide and nickel oxide. However, no passivation layer was observed on the surface of SUS316L nanoballs.

Table 5 shows the elemental composition of SUS316L nanoballs measured using TEM-EDS. The measurement was taken at the center and the surface of the nanoball. Apparently the oxide content at the center is significantly higher than the oxide content at the surface. This would explain the lack of a passivation layer on the nanoball surface and the difference in the diffraction pattern of the center and surface of the nanoball. However, Figure 3-7 shows the presence of satellite nanoballs surrounding larger nanoballs. The TEM-EDS measurements could therefore have been affected by the presence of the satellite nanoballs that had higher oxide contents.

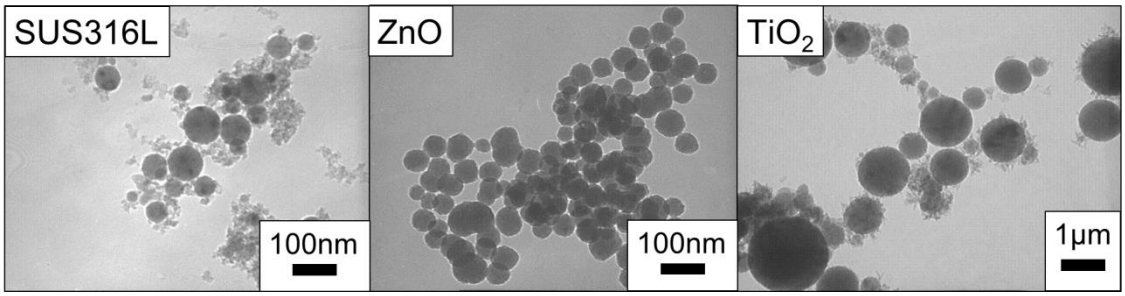

Figure 3-5 TEM images of (a) SUS316L, (b) ZnO and (c) TiO_2 nanoballs.

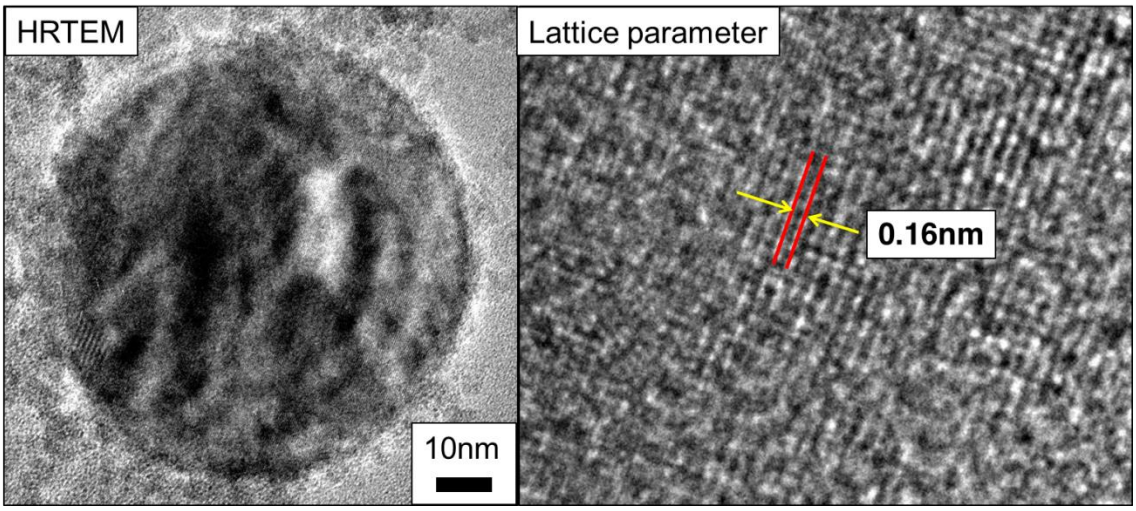

Figure 3-6 TEM image of SUS316L nanoball showing HRTEM and lattice parameter of its center.

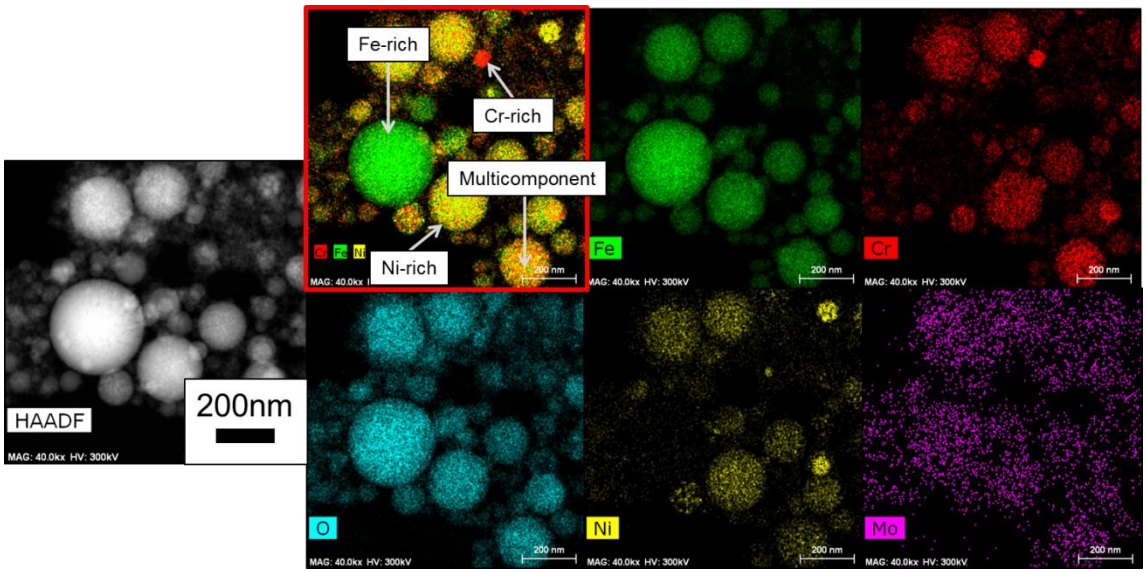

Figure 3-7 TEM-EDS image of SUS316L nanoballs showing the presence of distinct metallic oxide species such as iron oxide, chromium oxide and nickel oxide.

Table 5 TEM-EDS elemental composition of SUS316L nanoballs.

Element	**Mole percent (%)**	
	Nanoball center	**Nanoball surface**
Fe	63.35	92.33
Cr	1.85	5.17
Ni	1.19	2.21
O	33.52	0
Mo	0.09	0.38
Total	100	100

3.3 X-ray diffraction (XRD) results

Figure 3-8 shows the XRD results for the wires used as the cathode for nanoballs synthesis. Generally, for wires made out of pure metals, the oxide content was expected to be very low (less than 0.05%. of the total elemental composition). However, in Ti wire, the presence of photocatalytically active compounds, namely anatase and rutile, were detected.

Figure 3-9 shows the XRD results of the nanoballs. In terms of peak intensities, FeO, Fe_2O_3 and Cr_2O_3 were the main characteristic peaks present in the case of SUS316L nanoballs. ZnO characteristic peaks were present in the case of ZnO nanoballs. Anatase and brookite TiO_2 characteristic peaks were present in TiO_2 nanoballs. The presence of Fe_2O_3 and Cr_2O_3 in SUS3161L nanoballs contribute to its photocatalytic effect. The bandgap of Fe_2O_3 is 2.2 eV, while the bandgap of Cr_2O_3 is 3.6 eV. The low bandgap of these oxides causes them to become photocatalytically active when irradiated with UV light. As a comparison, the bandgap of anatase TiO_2 is 3.0 eV, which is much higher than the bandgap of Fe_2O_3 and Cr_2O_3. Even though the bandgap of the oxides in SUS316L nanoballs was lower than the bandgap of anatase TiO_2, SUS316L nanoballs decomposed MB at a slower rate than anatase TiO_2. The decomposition behaviour of MB in the presence of SUS316L, ZnO and TiO_2 nanoballs is shown in the photoabsorbance test results.

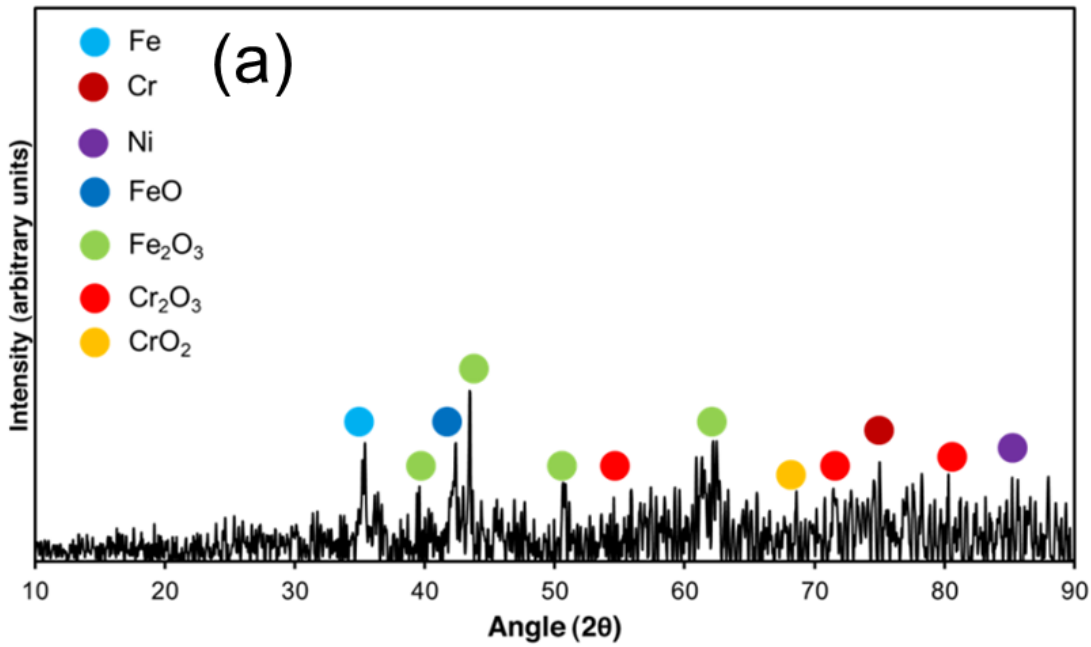
(a)
Fe
Cr
Ni
FeO
Fe2O3
Cr2O3
CrO2
Intensity (arbitrary units)
10
20
30
40
50
60
70
80
90
Angle (2θ)

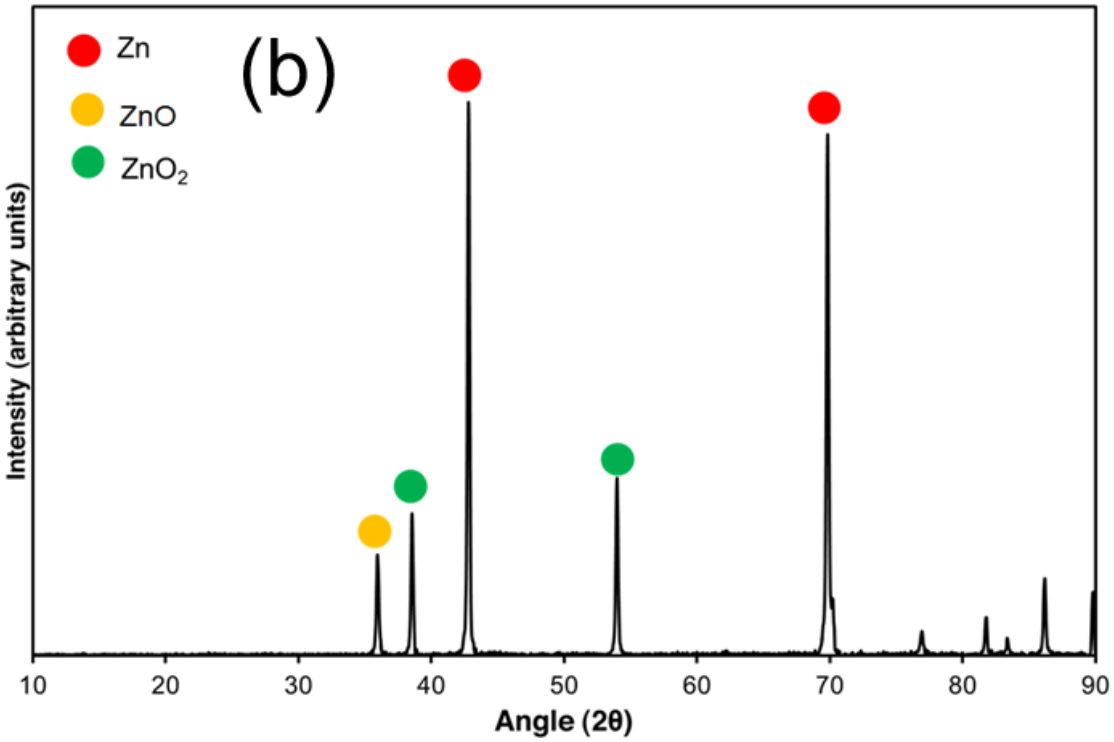
(b)
Zn
ZnO
ZnO2
Intensity (arbitrary units)
10
20
30
40
50
60
70
80
90
Angle (2θ)

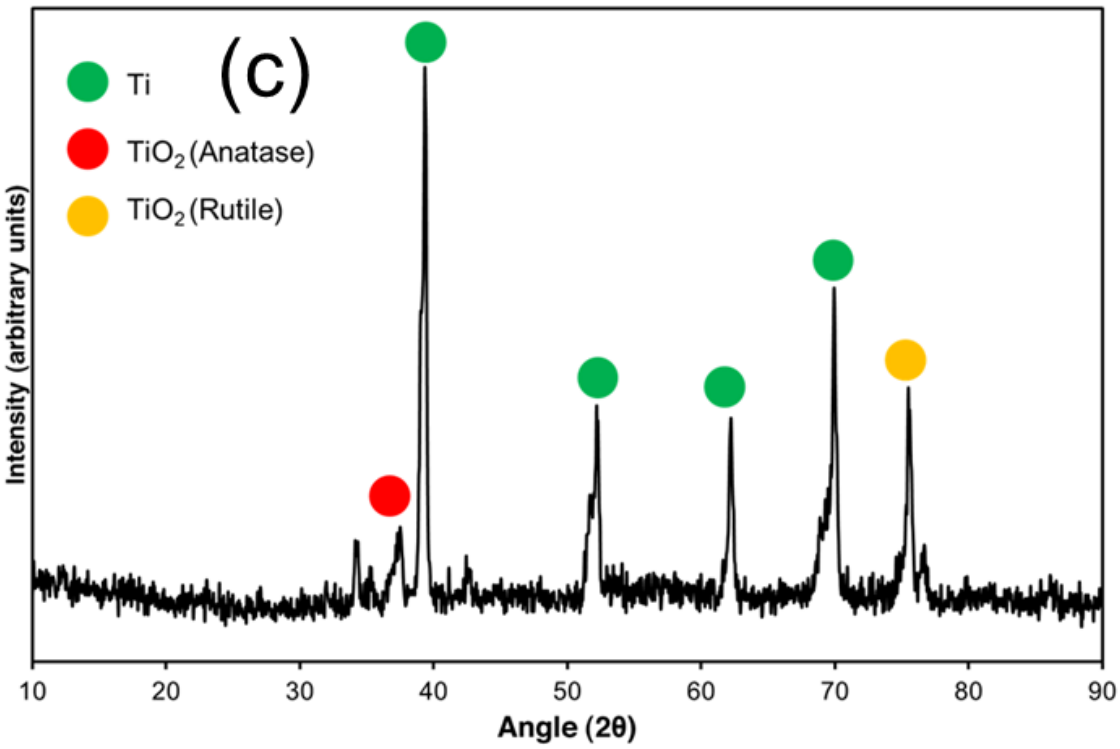

Figure 3-8 XRD spectra of (a) SUS316L, (b) Zn and (c) Ti wire.

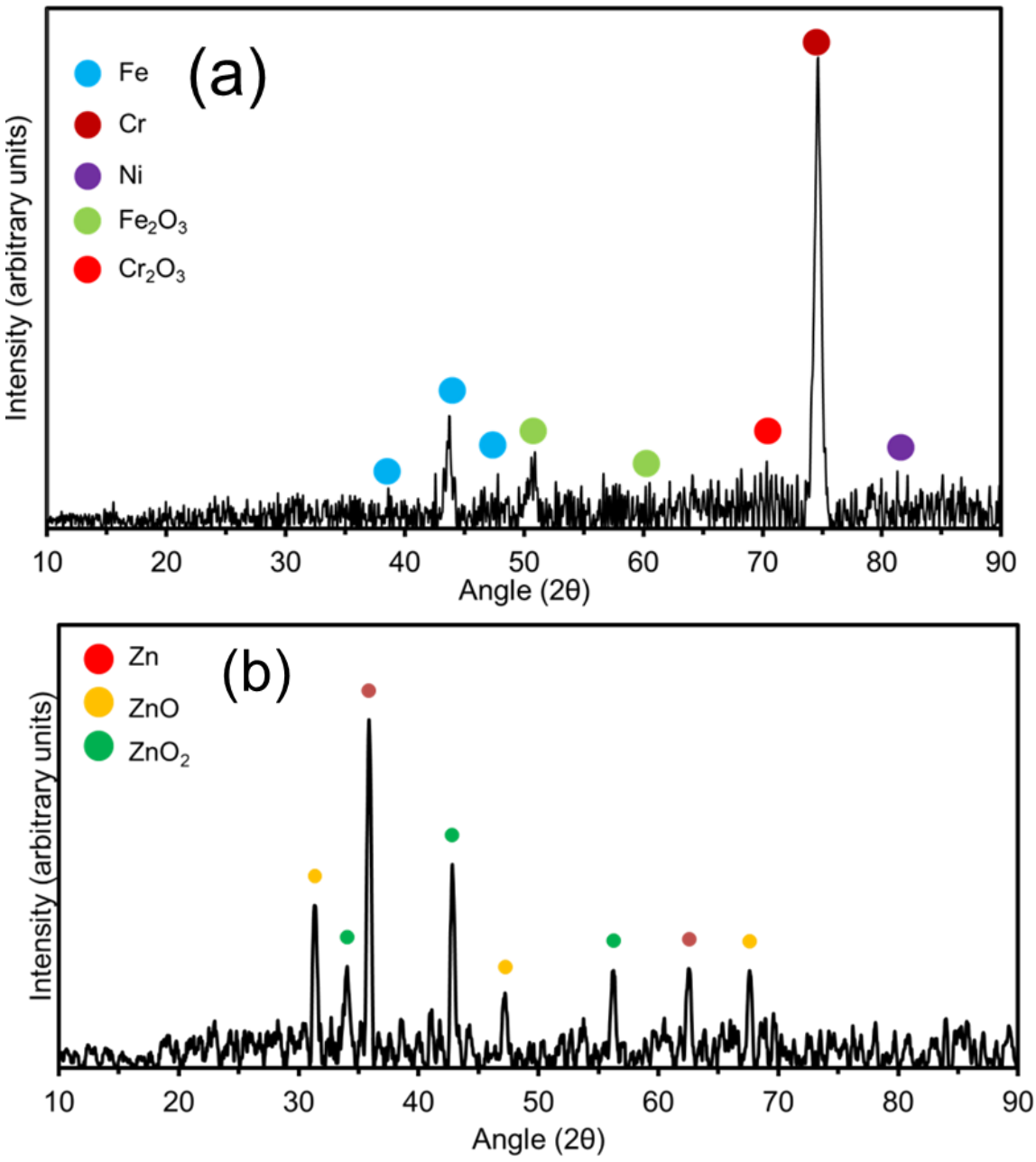
(a)
Fe
Cr
Ni
Fe_2O_3
Cr_2O_3
Intensity (arbitrary units)
10
20
30
40
50
60
70
80
90
Angle (2θ)
(b)
Zn
ZnO
ZnO_2
Intensity (arbitrary units)
10
20
30
40
50
60
70
80
90
Angle (2θ)

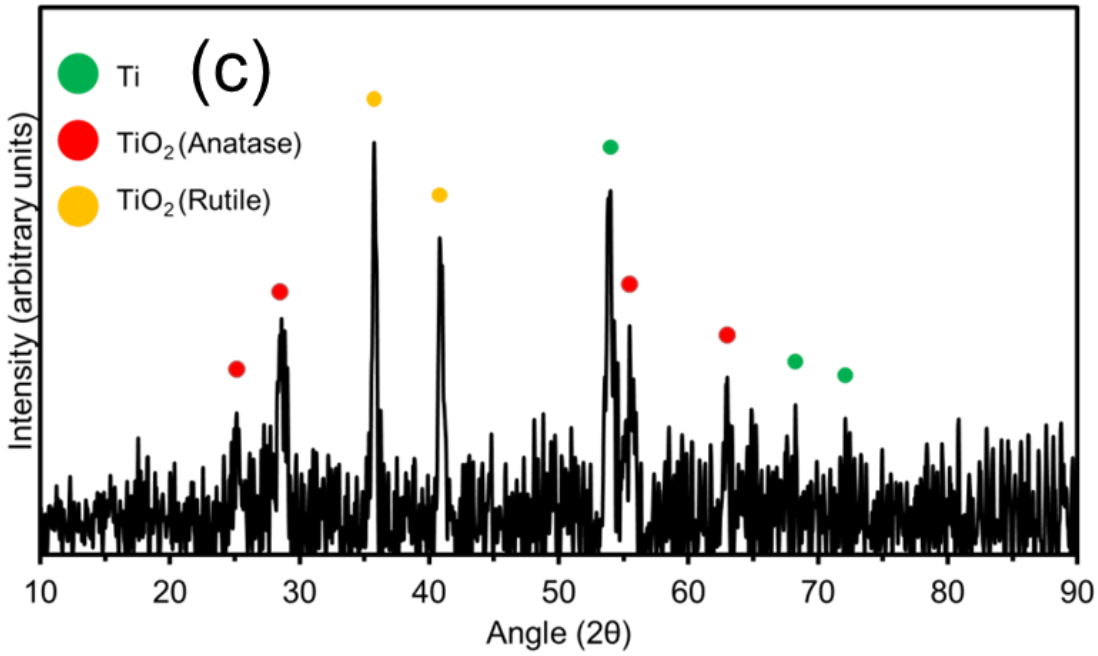

Figure 3-9 XRD spectra of (a) SUS316L nanoballs, (b) ZnO nanoballs and (c) TiO_2 nanoballs.

3.4 Nanoball yield evaluation

Table 6 shows the hourly yield of nanoballs after 3 hours of sustained glow-discharge plasma.

Table 6 Yield of nanoballs after three hours of continuous glow-discharge.

Nanoball type	**Mass (g)**
ZnO	0.010
TiO_2	0.009
SUS316L	0.017

In terms of yield, SUS316L nanoballs had the highest yield, followed by ZnO and TiO_2 nanoballs. The high voltage needed to initiate and sustain glow-discharge plasma contributed to the high yield of SUS316L nanoballs. When the voltage was increased, the effect of current concentration, and thus Joule heating was increased, causing more of the cathode surface to be melted at a given time.

3.5 Brunauer-Emmett-Teller (BET) results

Table 7 shows the results of BET measurement. BET measurement was used to determine the nanoballs surface area and pores volume. The table below show the results of BET measurements, where the surface area and pore volumes of ZnO, TiO_2 and SUS316L nanoballs were measured.

BET results show that ZnO had the largest surface area and pore volumes of all three types of nanoballs, followed by TiO_2 and SUS316L. The large surface area of ZnO nanoballs was consistent with its excellent photocatalytic ability, where it was able to decompose MB in a relatively short time compared to TiO_2 and SUS316L. Optimization of nanoballs synthesis is needed to produce smaller sized nanoballs with larger surface area; BET measurement shows that submerged glow-discharge has good potential to produce nanoballs with large surface area.

ZnO nanoballs had the largest surface area and pore volumes of all the three types of nanoballs, nearly double than the values measured on TiO_2 nanoballs. The large surface area of ZnO nanoballs was consistent with its excellent photocatalytic ability, where it was able to decompose MB in a relatively short time compared to TiO_2 and SUS316L. Although SUS316L nanoballs had the lowest surface area and pore volume compared to ZnO and TiO_2 nanoballs, the measurements indicate that the surface area and pore volume of SUS316L are similar to that of TiO_2 nanoballs.

Figure 3-10 shows the results of particle size distribution estimation using Mac-View software. It was used to estimate the average surface areas, average circumferences and diameters of the nanoballs. The graphs show

that in terms of size distribution, ZnO had an even distribution, where the sizes of the nanoballs fall within a relatively narrow range (approximately 100±20nm). This means that the glow-discharge voltage for ZnO synthesis (95V) was the optimal voltage because it produced nanoballs that are consistently-sized.

On the other hand, TiO_2 and SUS316L nanoballs had a wider range of sizes compared to ZnO nanoballs, approximately 100±40nm for TiO_2 and 100±60nm for SUS316L. This means that in terms of size distribution, the glow-discharge voltages for TiO_2 and SUS316L needs to be refined further so that consistently-sized nanoballs can be produced. This can be achieved by either increasing the glow-discharge voltage or filtering the nanoballs solutions after synthesis and centrifuging.

Table 8 shows the average surface area and particle sizes (circumference and diameter). These values were measured using the TEM images of the nanoballs. According to the results, TiO_2 nanoballs had the largest surface area, followed by ZnO and SUS316L nanoballs. These results confirm the findings from BET measurements. However there was a slight difference in terms of average surface areas and particle size, particularly between TiO_2 and ZnO.

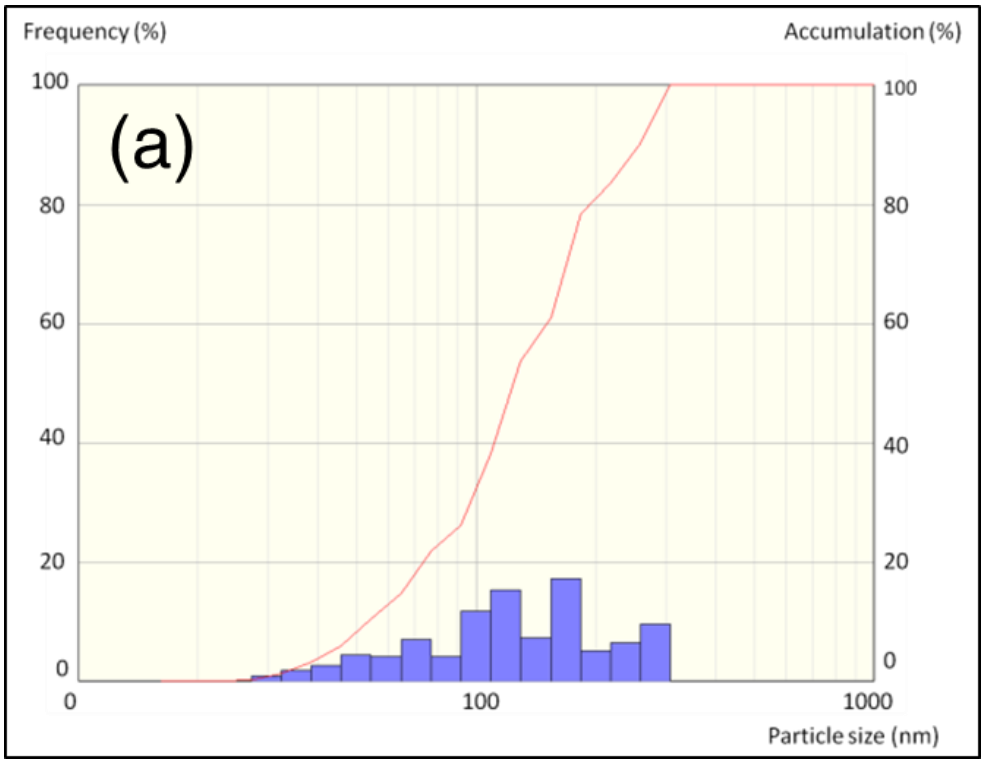
Frequency (%)
Accumulation (%)
(a)
100
80
60
40
20
0
0
100
1000
Particle size (nm)

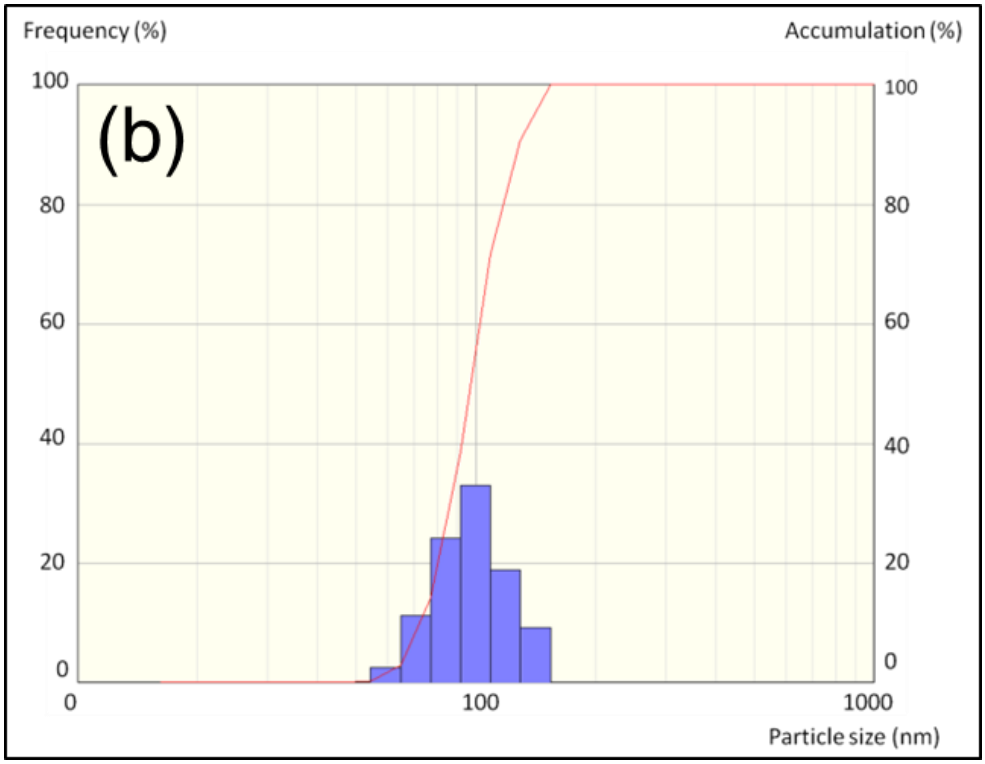
Frequency (%)
Accumulation (%)
(b)
100
80
60
40
20
0
0
100
1000
Particle size (nm)

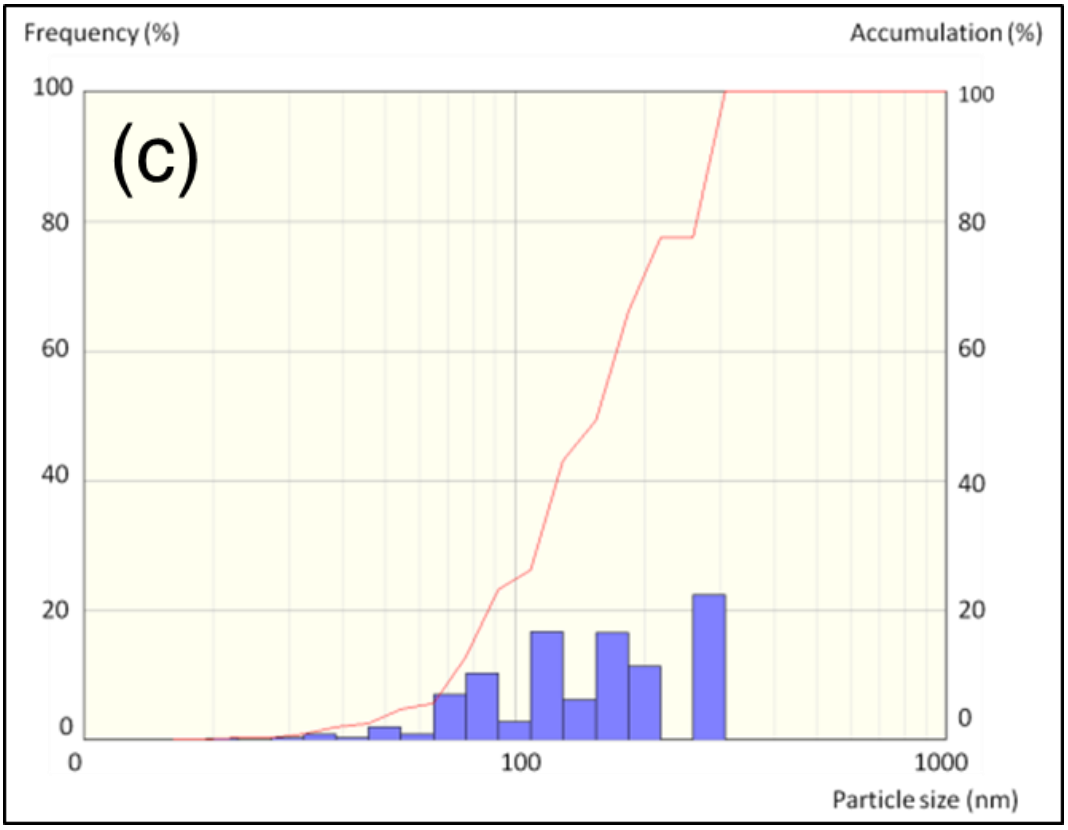

Figure 3-10 Particle size distribution of (a) SUS316L nanoballs, (b) ZnO nanoballs and (c) TiO_2 nanoballs.

Table 7 Surface area and total pore volume of the nanoballs measured using BET.

Nanoball type	**Surface area (m^2/g)**	**Total pore volume (cm^3/g)**
ZnO	115.4	0.1931
TiO_2	67.69	0.08426
SUS316L	40.94	0.06587

Table 8 Average surface area, particle circumference and diameter estimation for the nanoballs.

Nanoball type	**Avg. surface area (nm^2)**	**Avg. particle circumference (nm)**	**Avg. particle diameter (nm)**
TiO_2	9615.35	301.0	95.80
ZnO	6151.42	272.2	86.63
SUS316L	3861.37	211.6	67.06

3.6 Conclusions

SUS316L, TiO_2 and ZnO nanoballs have been successfully synthesized via submerged glow discharge plasma. Submerged glow-discharge plasma easily synthesized alloyed nanoballs.

The wires used for submerged glow-discharge plasma as cathode material were composed of nearly pure metallic material, with very little oxygen content. The nanoballs that were synthesized from those wires contained significantly higher oxide content than the original wires.

This research has demonstrated the photocatalytic potential of the nanoballs, especially in the case of SUS316L nanoballs, where it was able to effectively decompose MB. The presence of photocatalytically active species such as Fe_2O_3 and Cr_2O_3 was confirmed in SUS316L nanoballs.

References

[1] T. K. Townsend, E. M. Sabio, N. D. Browning, F. E. Osterloh, Energy & Environmental Science, **4** (2011) 4270-4275.
[2] L. -S. Zhong, J. -S.Hu, H. -P. Liang, A. –M. Cao, W. –G. Song, L. –J. Wan, Advanced Materials, **18** (2006) 2426-2432.
[3] J. Ding, Q. Zhong, S. Zhang, Journal of Molecular Catalysis A: Chemical, **393** (2014) 222-231.
[4] A. Hakuli, M. E. Harlin, L. B. Backman, A. O. I. Krause, Journal of Catalysis, **184** (1999) 349-356.
[5] G. Guan, T. Kida, A. Yoshida, Applied Catalysis B: Environmental, **41** (2003) 387-396.
[6] A. K. Gupta, M. Gupta, Biomaterials, **26** (2005) 3995-4021.
[7] William W. Yu, Joshua C. Falkner, Cafer T. Yavuz and Vicki L. Colvin, Chemical Communications, **20** (2004) 2306-2307.
[8] P. A. Pekakis, N. P. Xekoukoulotakis, D. Mantzavinos, Water Research, **40** (2006) 1276-1286.
[9] P. S. S. Kumar, M. R. Raj, S. Anandan, Solar Energy Materials and Solar Cells, **94** (2010) 1783-1789.
[10] A. Paleologou, H. Marakas, N. P. Xekoukoulotakis, A. Moya, Y. Vergara, N. Kalogerakis, P. Gikas, D. Mantzavinos, Catalysis Today, **129** (2007) 136-142.
[11] K. J. Shieh et. al., Nanomed. Nanotech. Bio. Med., 2 (2006) 121-126.
[12] H. Gnaser, A. Orendorz, C. Ziegler, E. Rowlett, W. Bock, Solar Energy Materials and Solar Cells, **252** (2006) 6996-6999.
[13] J. W. Choi, S. E. Lee, B. G. Lee, Y. S. Jeong, H. J. Oh, C. S. Chi, Transactions of Nonferrous Metals Society of China, **19** (2009) 1027-1030.
[14] G. Saito, S. Hosokai, T. Akiyama, Materials Chemistry and Physics, **130** (2011) 79-83.
[15] A. A. Tahir, K. G. U. Wijayantha, Journal of Photochemistry and Photobiology A: Chemistry, **216** (2010) 119–125.
[16] A. Lei, B. Qu, W. Zhou, Y. Wang, Q. Zhang, Bingsuo Zou, Materials Letters, 66 (2011) 72-75.
[17] S. Saremi-Yarahmadi, A. A. Tahir, B. Vaidyanathan, K. G. U. Wijayantha, Materials Letters, **63** (2009) 523-526.
[18] S.C. Kwon, M. Fana, T.D. Wheelock, B. Saha, Separation and Purification Technology, **58** (2007) 40–48.

[19] A. A. Tahir, K. G. U. Wijayantha, S. Saremi-Yarahmadi, M. Mazhar, V. McKee, Chemistry of Materials, **21** (2009) 3763–3772.
[20] V. R. Satsangi, S. Kumari, A. P. Singh, R. Shrivastav, S. Dass, International Journal of Hydrogen Energy, **33** (2008) 312 – 318.
[21] S. Boumaza, A. Boudjemaa, S. Omeiri, R. Bouarab, A. Bouguelia, M. Trari, Solar Energy, **84** (2010) 715–721.
[22] M.A. Gondal, A. Hameed, Z. H. Yamani, A. Suwaiyan, Applied Catalysis A: General, **268** (2004) 159–167.
[23] T. J. LaTempa, X. Feng, M. Paulose, C. A. Grimes, Journal of Physical Chemistry C, **113** (2009) 16293–16298.
[24] N. J. Cherepy, D. B. Liston, J. A. Lovejoy, H. Deng, J. Z. Zhang, Journal of Physical Chemistry B, **102** (1998) 770-776.
[25] M.I. Dominguez, M. Sanchez, M.A. Centeno, M. Montes, J.A. Odriozola, Journal of Molecular Catalysis A: Chemical, 277 (2007) 145–154.
[26] M.I. Dominguez, M. Sanchez, M.A. Centeno, M. Montes, J.A. Odriozola, Applied Catalysis A: General, **302** (2006) 96–103.

Chapter 4 Experimental Results and Discussion: Nanoballs photocatalytic activity

Chapter 4 Experimental results and discussion: Photocatalytic activity of nanoballs

4.1 Photoabsorbance test results MB and PNDA

Figure 4-1 shows the photographs taken from photocatalytic effect test on TiO_2, ZnO and SUS316L nanoballs For all nanoballs, UV-irradiation has been done for at least 24 hours. Every six hours, a photograph of the container containing the MB and nanoball mixture is taken. This is to provide visual proof on the degradation of MB dye. Degradation is exhibited through the fading of the dye; as the dye is faded, the blue color of the dye disappears causing the dye solution to become transparent.

In case of TiO_2 and ZnO nanoballs, the dye solution faded gradually for the whole duration of UV-irradiation. The fading began soon after UV-irradiation, as can be seen from the sixth-hour photograph. As the UV-irradiation time increased, the blue color of the dye faded more until 24 hours has been reached. The maximum fading therefore occurred at the end of the UV-irradiation, as evidenced by the photoabsorbance test results.

In the case of SUS316L nanoballs, there was no significant color fading occurring in 24 hours. However, when the UV-irradiation time was increased to 72 hours, the dye solution became nearly transparent. This showed that SUS316L nanoballs were able to decompose the dye solution although it took a longer time than TiO_2 and ZnO nanoballs. The decomposition of MB was confirmed in the photoabsorbance test of SUS316L nanoballs, where the peak of MB was reduced to nearly baseline

level after 72 hours of UV-irradiation. Therefore, these results indicate that SUS316L nanoballs also have photocatalytic activity when irradiated with UV-light.

Figure 4-2 shows the photoabsorbance test results after MB decomposition in presence of nanoballs. MB peak intensity was reduced by mixing with these nanoballs while UV light was irradiated onto the photocatalytic test set-up. shows the absorbance in the case of ZnO nanoballs present in the mixture of MB. The characteristic peaks of MB at 290 and 650 nm became lower than initial height after UV-irradiation, indicating the decomposition of MB has occurred. The characteristic peaks of MB were also reduced in intensity in the case of SUS316L and TiO_2 nanoballs, as shown in. MB was effectively decomposed in the presence of all three types of nanoballs. ZnO decomposed MB the fastest, followed by TiO_2 and SUS316L nanoballs. Mass spectroscopy showed that for TiO_2 and ZnO nanoballs, MB was decomposed directly into lighter molecules within 24 hours.

Figure 4-3 shows the photoabsorbance test results of PNDA photodecomposition in presence of the nanoballs under UV irradiation. In Figure 4-3 (a), SUS316L nanoballs only showed significant $\cdot OH$ radicals generation after 72 hours of UV-irradiation. In Figure 4-3 (b), ZnO nanoballs caused the characteristic peak of PNDA to reduce to baseline gradually in 24 hours. This is consistent with the near-complete photodecomposition of MB in ZnO nanoballs case. However, in Figure 4-3 (c), TiO_2 nanoballs did not show much decrease for PNDA characteristic

peaks in 24 hours, despite TiO_2 nanoballs having similar photocatalytic performance as ZnO nanoballs. The low amounts of photocatalytically active species, which is anatase, in TiO_2 nanoballs might have caused it to show less PNDA degradation.

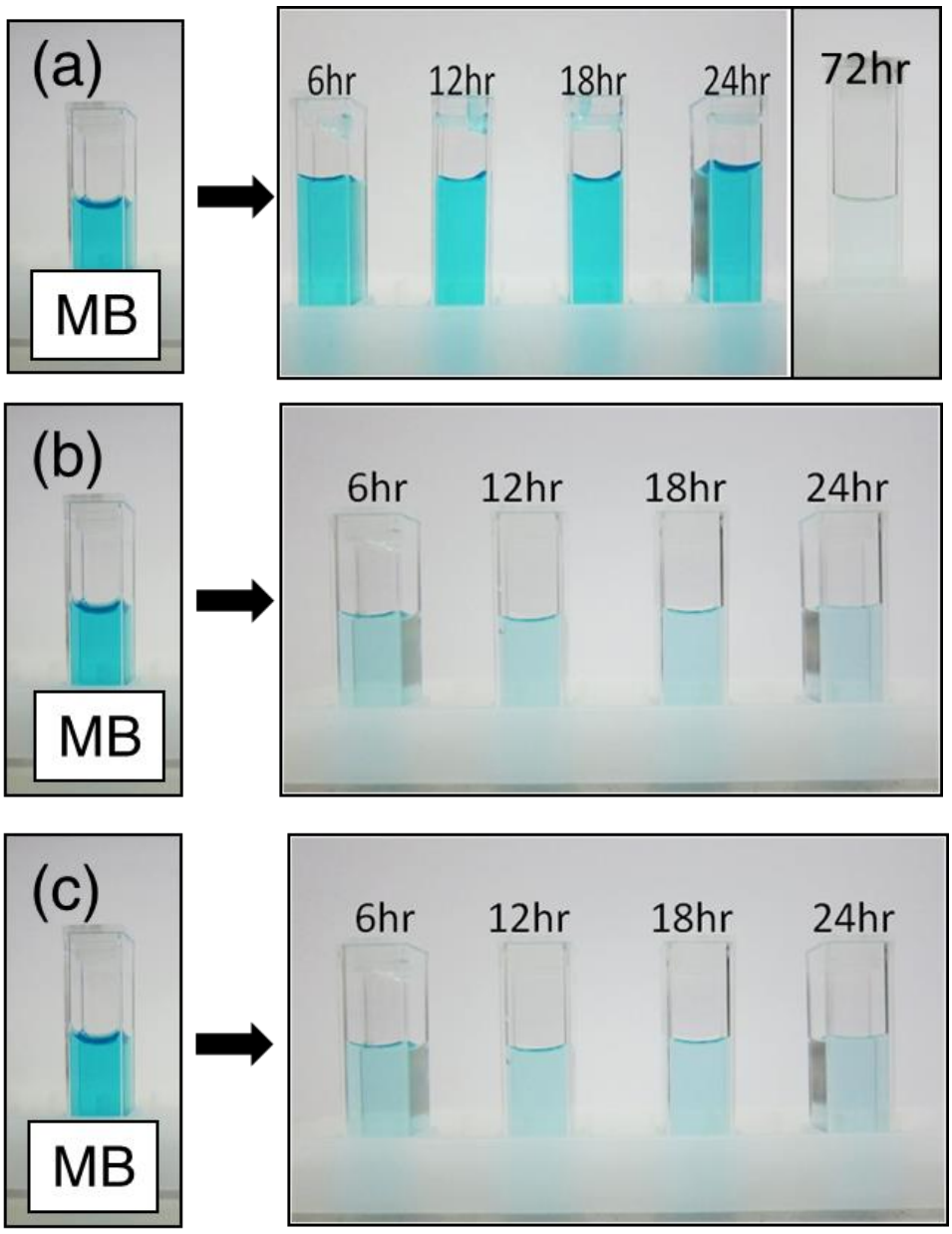

Figure 4-1 Photocatalytic test photos of the mixture of MB solution in (a) SUS316L nanoballs, (b) ZnO nanoballs and (c) TiO_2 nanoballs under UV light irradiation.

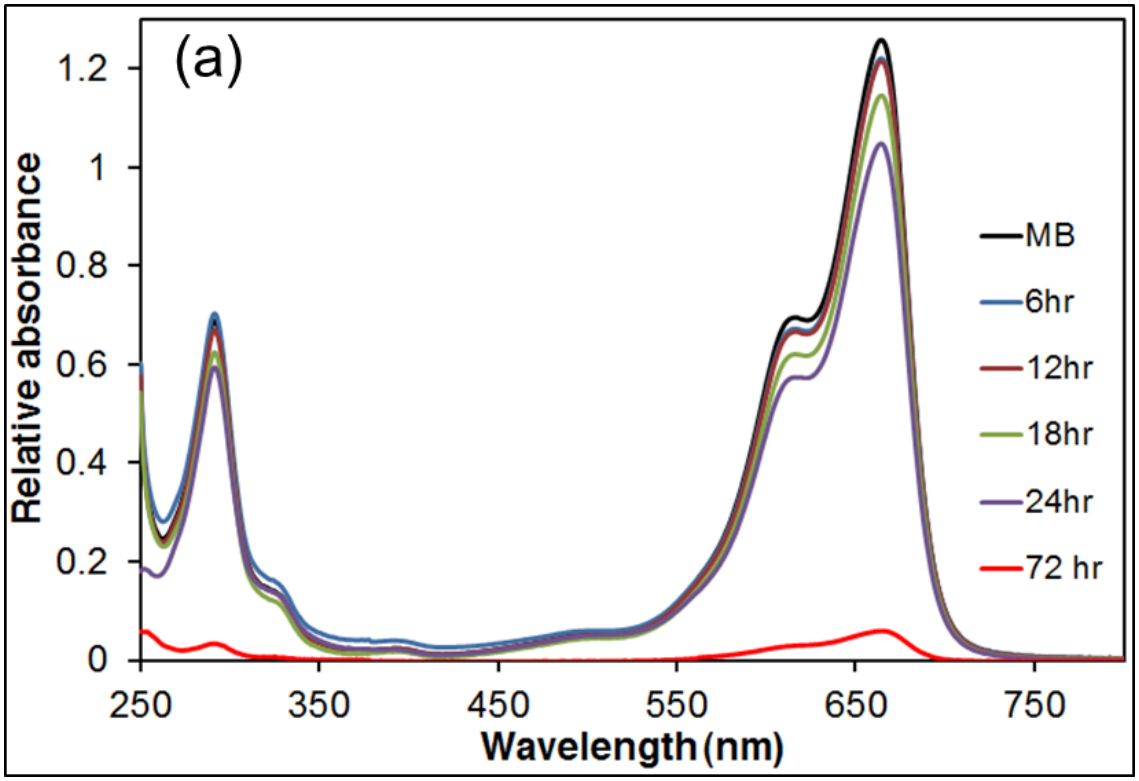
(a)
Relative absorbance
1.2
1
0.8
0.6
0.4
0.2
0
250
350
450
550
650
750
Wavelength (nm)
MB
6hr
12hr
18hr
24hr
72 hr

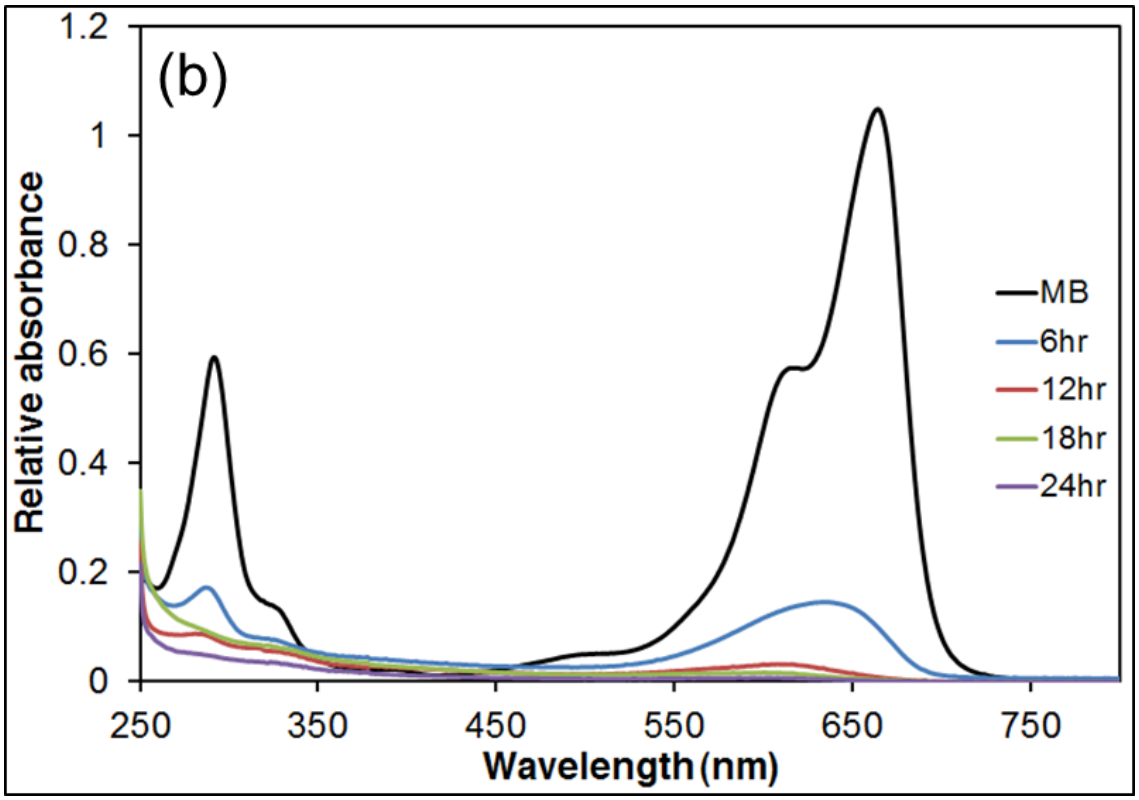
(b)
Relative absorbance
1.2
1
0.8
0.6
0.4
0.2
0
250
350
450
550
650
750
Wavelength (nm)
MB
6hr
12hr
18hr
24hr

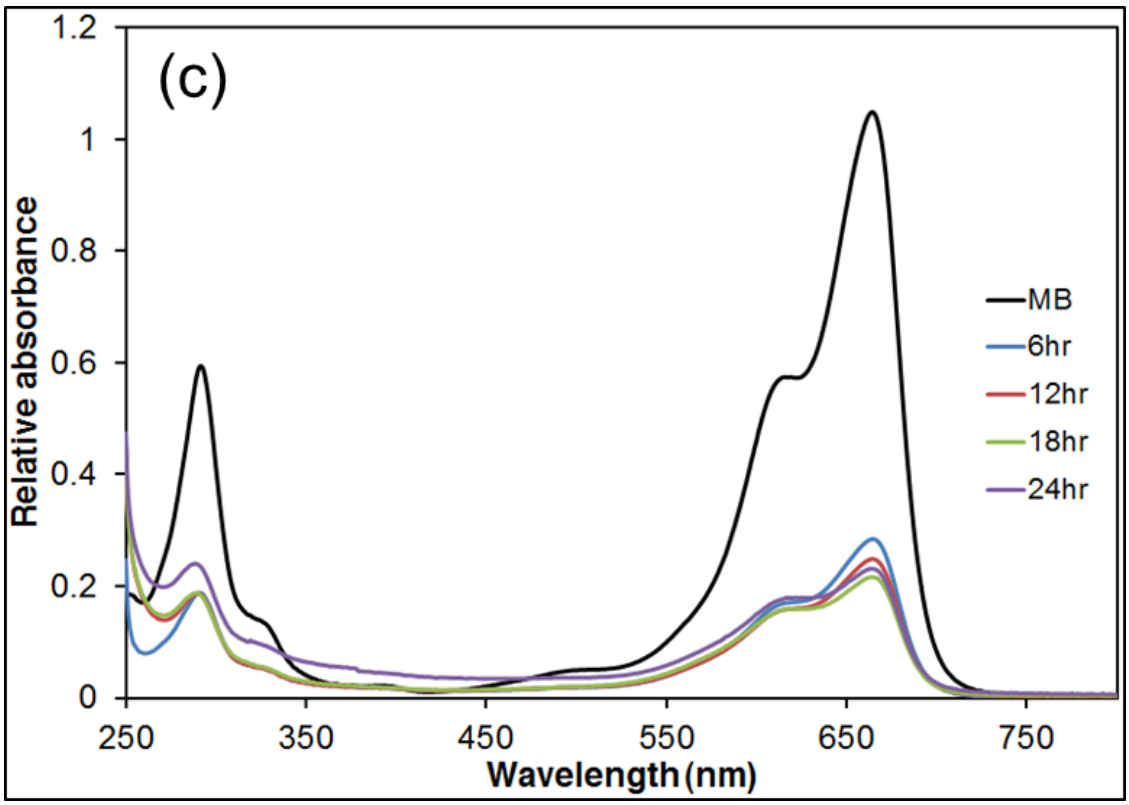

Figure 4-2 Photoabsorbance results for MB photodecomposition in presence of (a) SUS316L nanoballs, (b) ZnO nanoballs and (c) TiO_2 nanoballs under UV light irradiation.

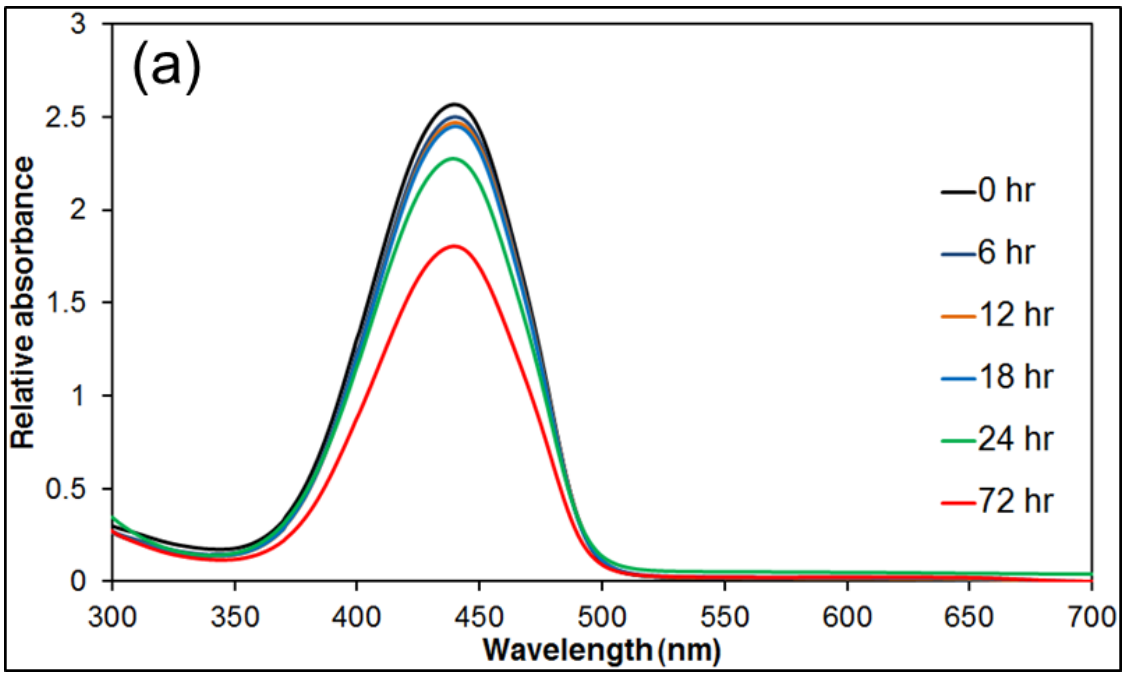
(a)
Relative absorbance
Wavelength (nm)
0 hr
6 hr
12 hr
18 hr
24 hr
72 hr

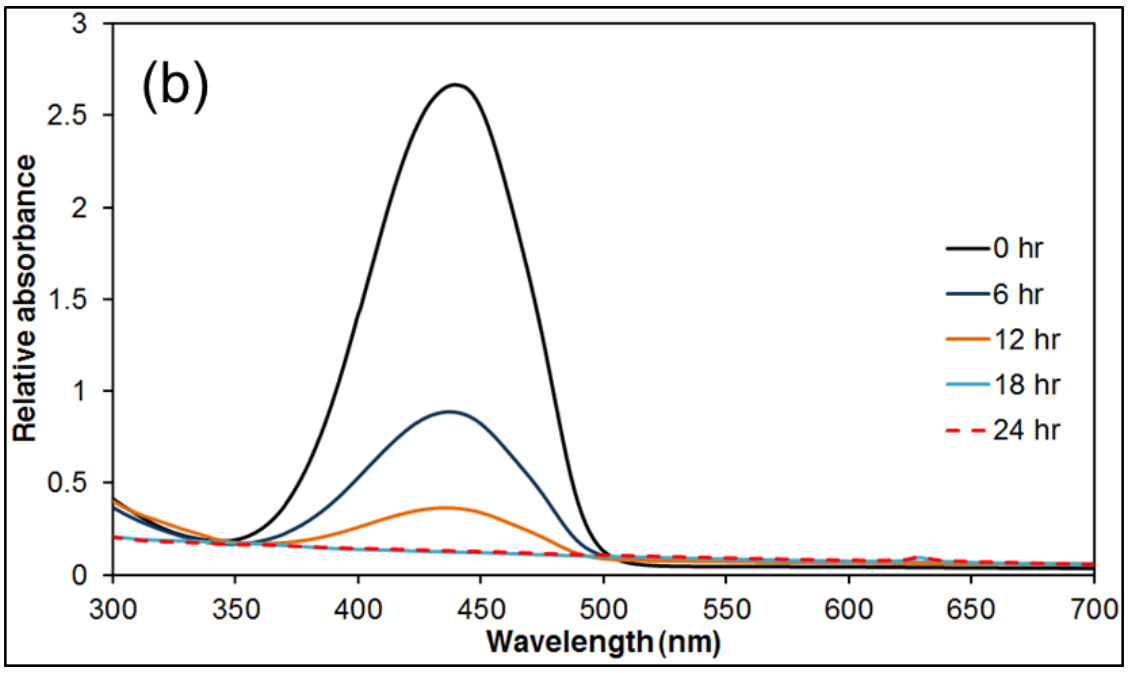
(b)
Relative absorbance
Wavelength (nm)
0 hr
6 hr
12 hr
18 hr
24 hr

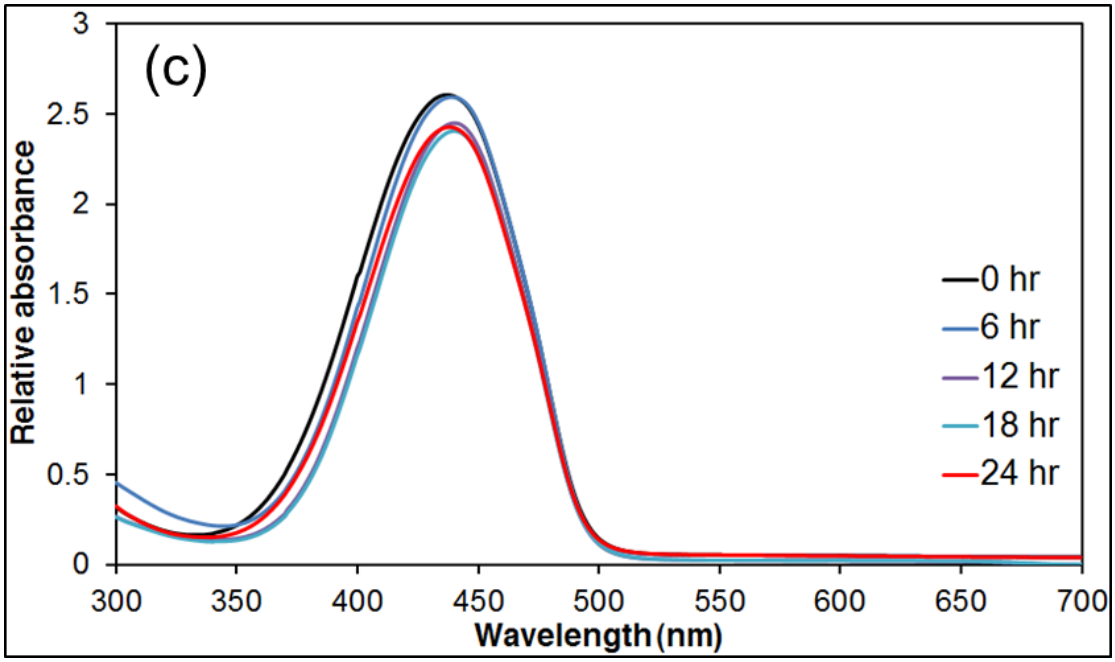

Figure 4-3 Photoabsorbance results for PNDA photodecomposition in presence of (a) SUS316L, (b) ZnO and (c) TiO_2 nanoballs under UV light irradiation.

4.2 Evaluation of photodecomposition rates and constants

Figure 4-5 shows the graph of the degradation rate of MB over 24 hours of UV-irradiation. ZnO showed the fastest degradation rate, whereas TiO_2 was the second fastest and SUS316L was the slowest. However, if the irradiation time is increased to 72 hours, SUS316L was able to degrade MB to baseline level. This can be seen in Figure 4-6 (b). These results indicate that even though the degradation rate of MB in presence of SUS316L nanoballs was slower than in TiO_2 or ZnO nanoballs, photocatalysis also occured in presence of SUS316L nanoballs. UV-irradiation of MB itself without any nanoballs for 72 hours revealed negligible degradation when compared the degradation in presence of the synthesized nanoballs.

The decomposition constants of each type of nanoballs have been calculated, and the results are shown in Table 9. The graph was plotted using logarithmic scale as shown in Figure 4-7, and the equation for decomposition constant was as follows:

$$I(t) = I_0 e^{-\mu t}$$

Figure 4-4 Equation describing the derivation of decomposition constant μ.

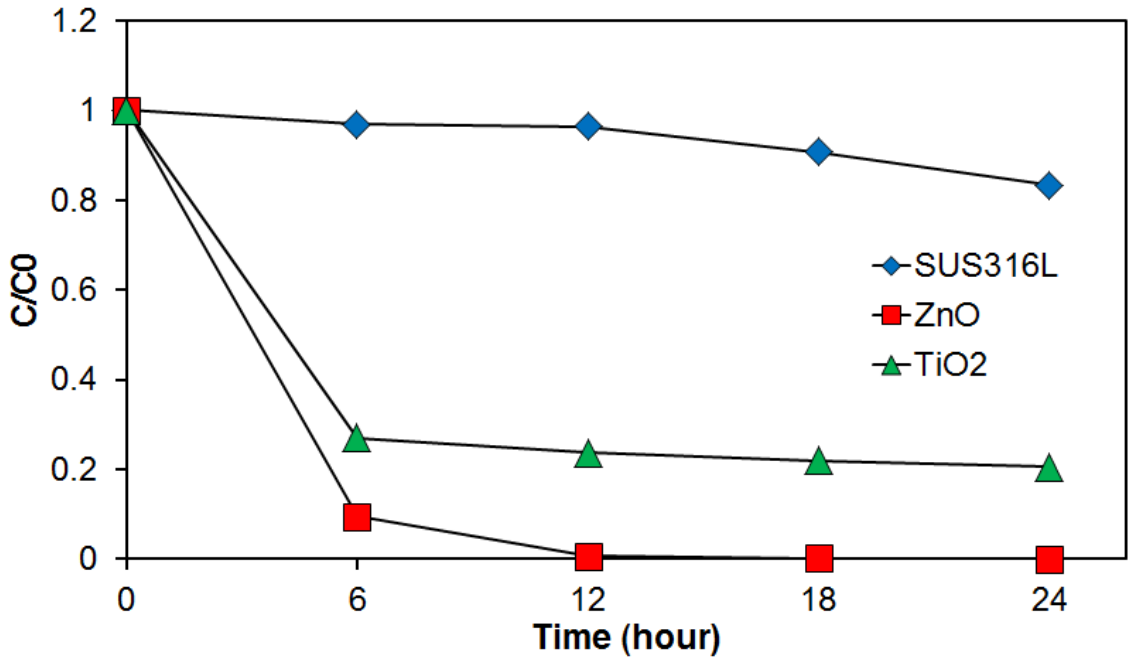

Figure 4-5 Photodecomposition behavior of MB in presence of SUS316L, ZnO and TiO_2 nanoballs within 24 hours.

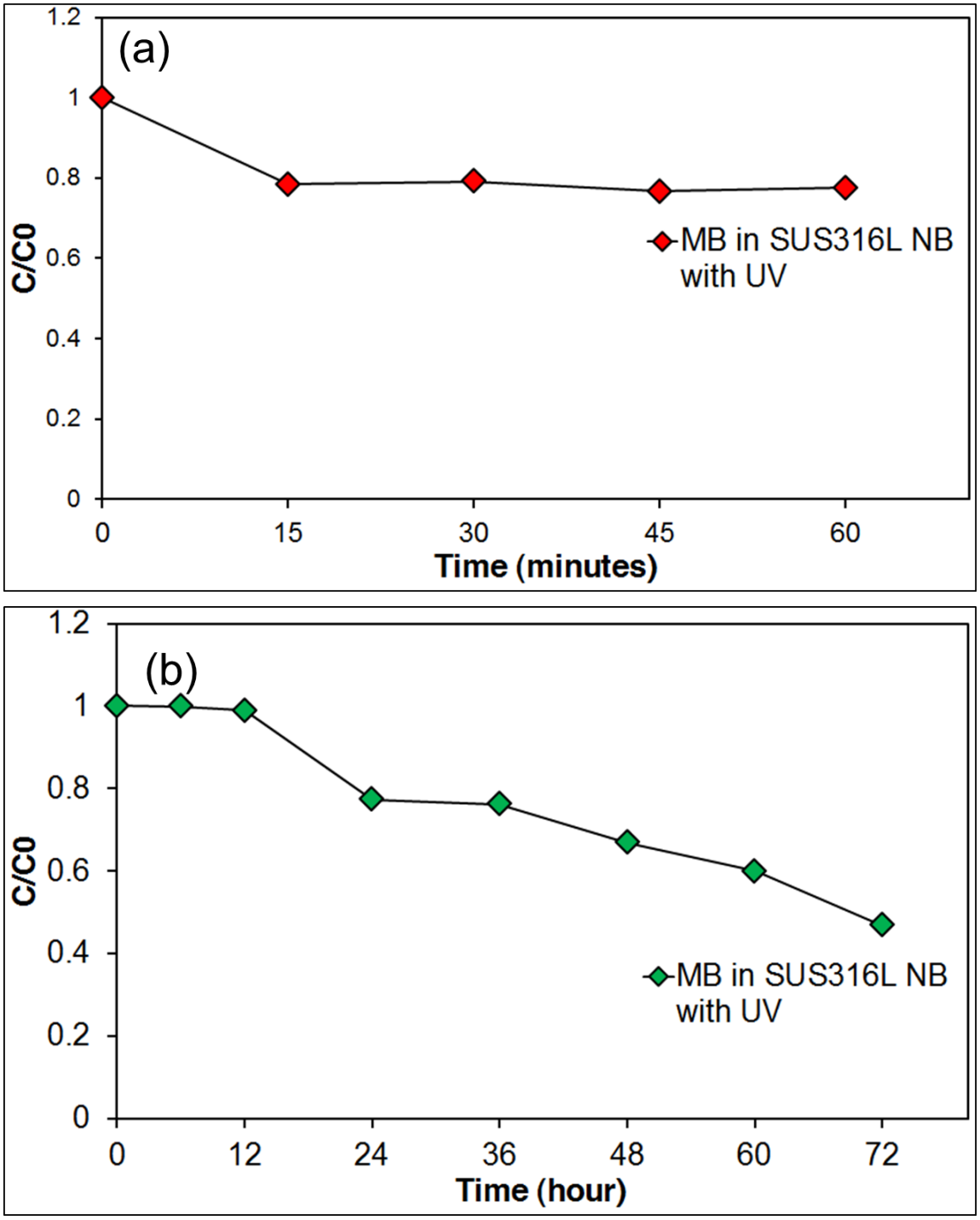

Figure 4-6 Photodecomposition behavior of MB in presence of SUS316L nanoballs within (a) 1 hour and (b) 72 hours.

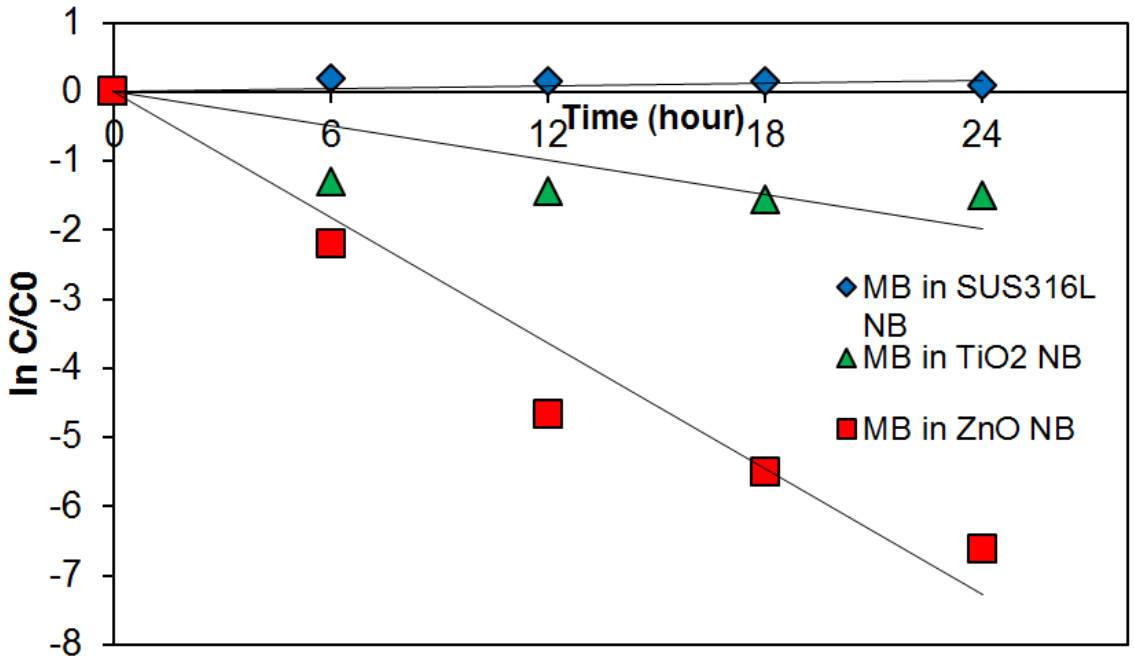

Figure 4-7 Photodecomposition behavior of MB in presence of SUS316L, ZnO and TiO_2 nanoballs, showing decomposition rate constants.

Table 9 Decomposition constants for photodecomposition of MB under UV light irradiation in presence of the nanoballs.

Nanoball type	**Decomposition constant (hr^{-1})**
ZnO	0.2892
TiO_2	0.056
SUS316L	0.0071

4.3 Mass spectrometry results

Figure 4-8 shows the mass spectroscopy results of the decomposition of MB. According to their mass-to-charge ratio (m/z), the by-products of MB decomposition can be identified. Generally, the intensities of MB (m/z = 284.13) were reduced in all three types of nanoballs. Mass spectroscopy has shown that by-products such as aminobenzenesulfonic acid (m/z = 176.88), benzenosulfonic acid (m/z = 152.92) and phenol (m/z = 94.93) were detected after 24 hours of UV-irradiation in TiO_2 and ZnO nanoballs and after 6 hours of UV-irradiation in SUS316L nanoballs. Additionally, 1-benzyl-4-phenyl-1H-1,2,3-triazole (m/z = 236.08), 2-ethylcyclohexanol (m/z = 128.96) and 1- methoxy-2-methyl-1-oxo-2-propanyl (m/z = 100.8) were detected after 24 hours of UV irradiation in SUS316L nanoballs. This showed that decomposition of MB has occurred in the presence of the nanoballs while UV-irradiation was applied.

The peak for MB (m/z = 284.13) was reduced after UV-irradiation in presence of photocatalytic nanoballs because the chemical bonds inside MB are broken. The breakage of bonds occur as the free radicals that are released after the action of UV light on the nanoball surfaces attack the bonds, severing the connection between the monomers of MB. The physical effect of MB peak reduction is its decolorization. Decolourization caused the blue color of the dye to fade, and finally the dye solution became transparent.

As a result of the bond breakage, the overall mass of MB within the solution was reduced. At the same time, the masses of decomposition by-products increased as the overall mass of MB was reduced. The peaks of the by-products were detected in all three cases from (b)-(d). The names of the decomposition by-products that were detected are listed in the table below.

In case of ZnO and TiO_2 nanoballs, the decomposition process occurred in a straightforward manner. Over the period of 24 hours, MB was gradually decomposed into lighter products. This was evidenced by the appearance of the peaks of MB by-products in the sixth hour graphs. At 24 hours, the peak of MB did not appear in ZnO. In case of TiO_2, the peak of MB at 24 hours still appeared, but its concentration was greatly reduced compared to before UV-irradiation.

In case of SUS316L nanoballs, the decomposition process occurred differently compared to ZnO and TiO_2. First it was oxidized into sulfoxide (m/z = 301), then it was reduced/decomposed into lighter products. This process is evidenced by the above mass spectroscopy data, where the sulfoxide peak appeared in the sixth hour graph. The rest of the peaks however are similar to the peaks that appeared in case of decomposition occurring in ZnO and TiO_2 nanoballs. After 24 hours of UV-irradiation, the peak of MB did not appear, while the peak for sulfoxide still increased. At the same time, the peaks of the decomposition by-products also increased at 24 hours.

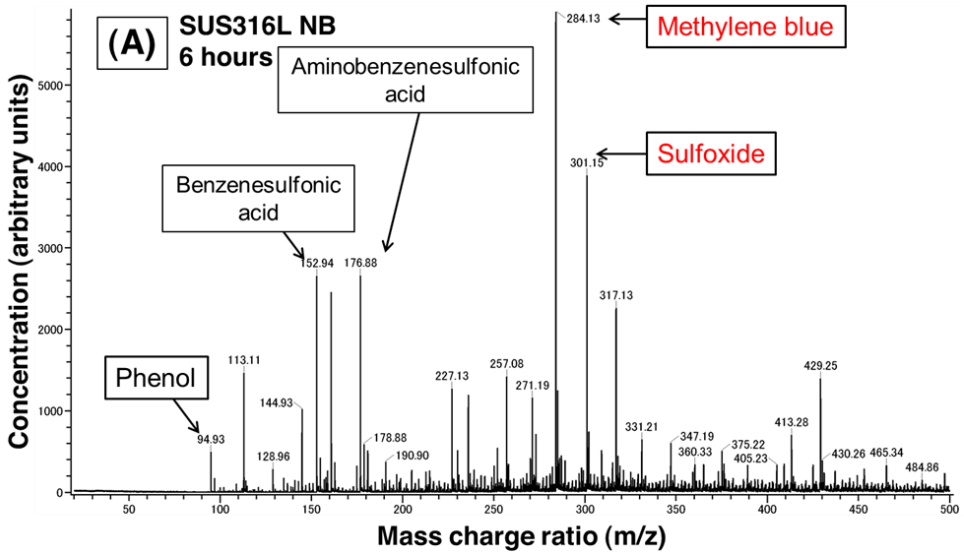
(A)
SUS316L NB
6 hours
Aminobenzenesulfonic acid
Benzenesulfonic acid
Phenol
Methylene blue
Sulfoxide
284.13
301.15
317.13
52.94
176.88
113.11
144.93
94.93
128.96
178.88
190.90
227.13
257.08
271.19
331.21
347.19
360.33
375.22
405.23
413.28
429.25
430.26
465.34
484.86
Concentration (arbitrary units)
Mass charge ratio (m/z)

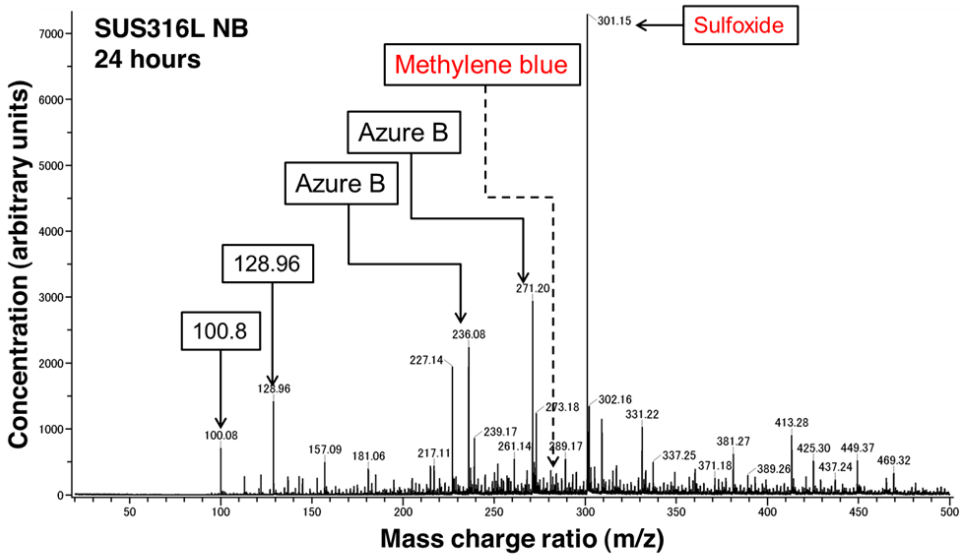
SUS316L NB
24 hours
Sulfoxide
Methylene blue
Azure B
Azure B
128.96
100.8
301.15
271.20
236.08
227.14
128.96
100.08
273.18
302.16
331.22
239.17
261.14
289.17
157.09
181.06
217.11
337.25
371.18
381.27
389.26
413.28
425.30
437.24
449.37
469.32
Concentration (arbitrary units)
Mass charge ratio (m/z)

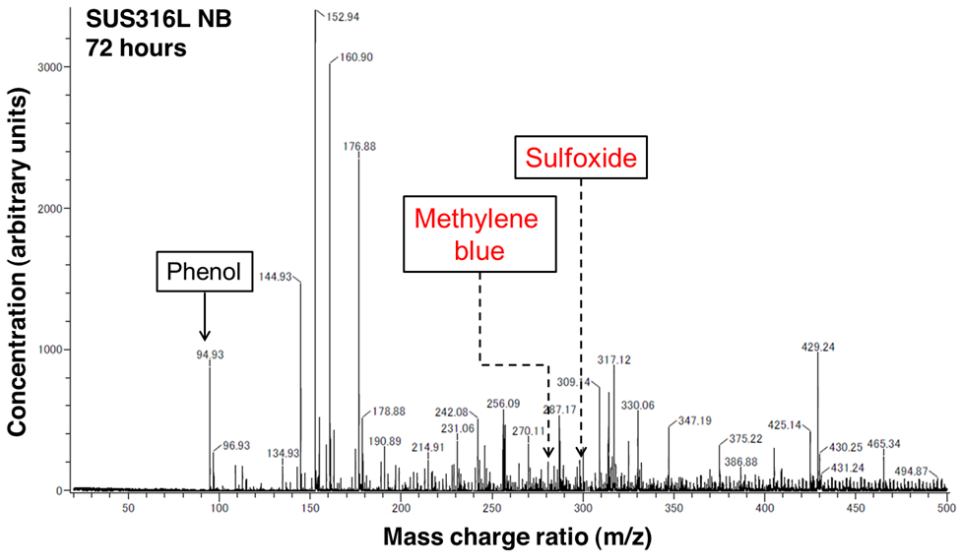
SUS316L NB
72 hours
Sulfoxide
Methylene blue
Phenol
152.94
160.90
176.88
144.93
94.93
96.93
134.93
178.88
190.89
214.91
231.06
242.08
256.09
270.11
287.17
309.14
317.12
330.06
347.19
375.22
386.88
425.14
429.24
430.25
431.24
465.34
494.87
Concentration (arbitrary units)
Mass charge ratio (m/z)

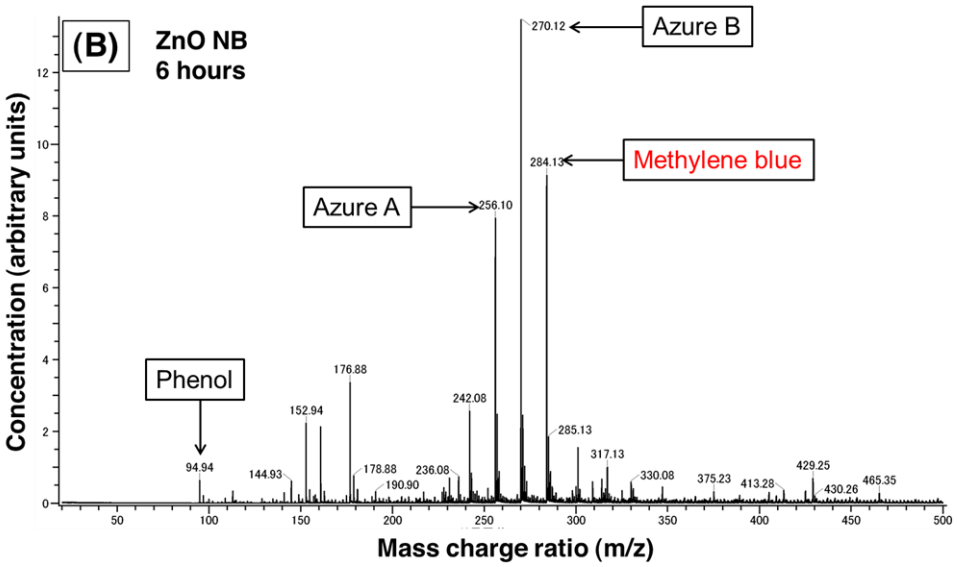
(B)
ZnO NB
6 hours
Azure B
Methylene blue
Azure A
Phenol
Concentration (arbitrary units)
Mass charge ratio (m/z)

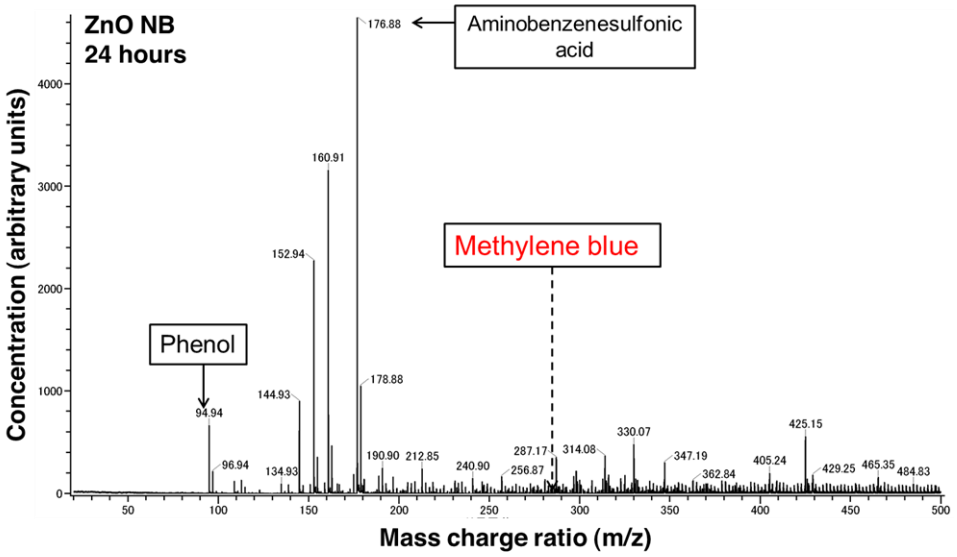
ZnO NB
24 hours
Aminobenzenesulfonic acid
Methylene blue
Phenol
Concentration (arbitrary units)
Mass charge ratio (m/z)

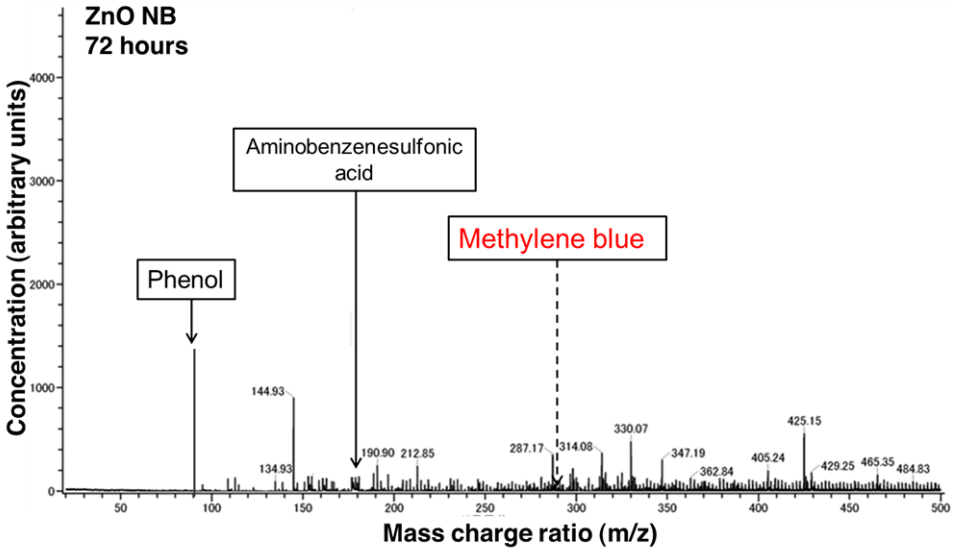
ZnO NB
72 hours
Aminobenzenesulfonic acid
Methylene blue
Phenol
Concentration (arbitrary units)
Mass charge ratio (m/z)

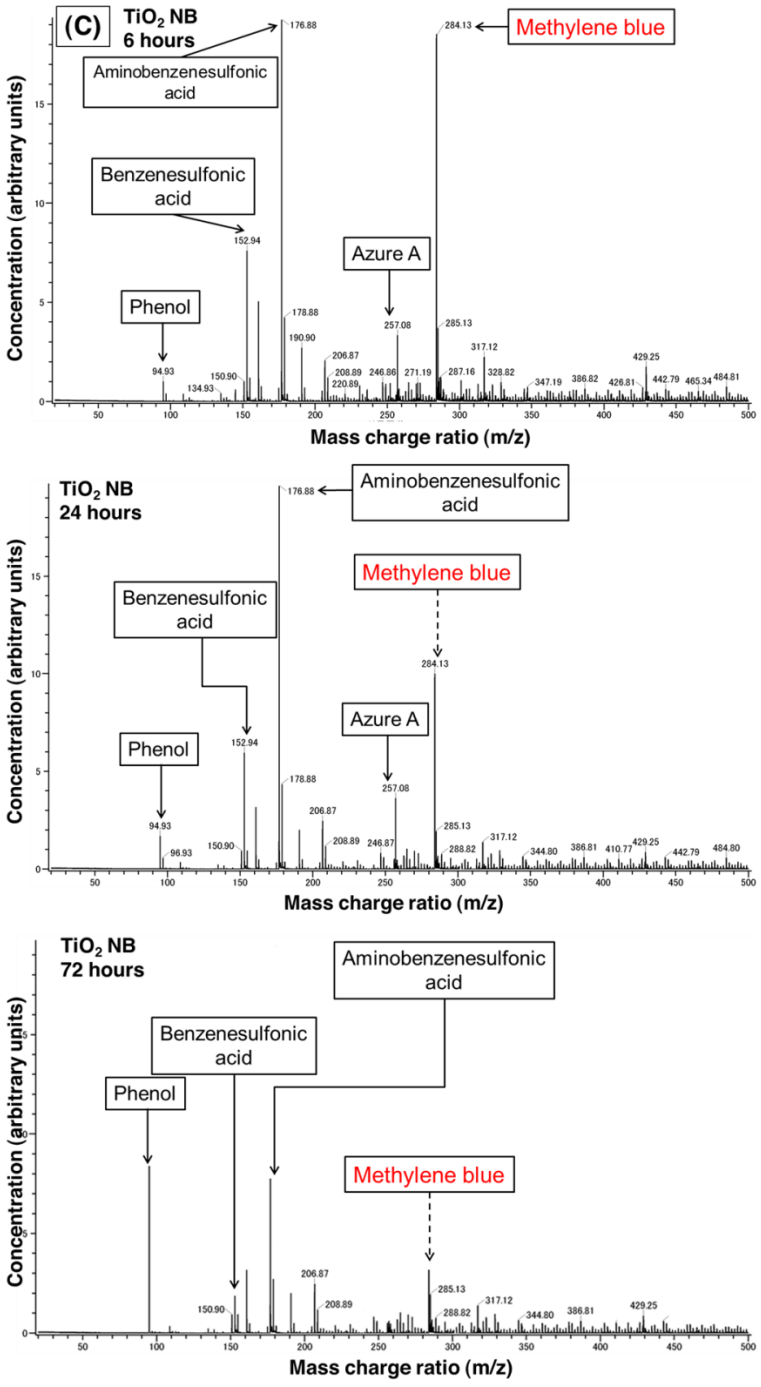

Figure 4-8 (a) Mass spectrometry of MB after 6, 24 and 72 hours of UV-irradiation in SUS316L nanoballs. (b) Mass spectrometry of MB after 6 and 24 hours of UV irradiation in ZnO nanoballs. (c) Mass spectrometry of MB after 6 and 24 hours of UV-irradiation in TiO_2 nanoballs.

Table 10 Byproducts of MB photodecomposition in each nanoballs under UV light irradiation.

m/z	**Molar mass (g/mol)**	**Name**	**Molecular formula**
301	330.0	Sulfoxide	$C_{17}H_{22}N_4SO$
284	319.9	Methylene blue	$C_{16}H_{18}N_3SCl$
270	305.8	Azure B	$C_{15}H_{16}ClN_3S$
256	291.8	Azure A	$C_{14}H_{14}ClN_3S$
230	-	5-acetamido-2-aminobenzenesulfonic acid	$C_8H_{10}N_2O_4S$
158	158.18	Benzenosulfonic acid	$C_6H_6O_3S$
136	-	N,N-dimethyl-P-phenylenediamine	$C_8H_{12}N_2$
94	94.11	Phenol	C_6H_6O

4.4 Mechanism of MB photodecomposition in presence of SUS316L nanoballs

The reaction that MB underwent in its decomposition in presence of SUS316L nanoballs is unique compared to the reactions in presence of TiO_2 or ZnO nanoballs [1-20]. In TiO_2 and ZnO, MB was decomposed directly into products with lower mass number. However, in presence of SUS316L nanoballs, MB was oxidized into sulfoxide first (m/z = 301), then decomposed into lighter products.

It is expected that O_2 and O^- were consumed during the photocatalytic reaction of MB in the presence of SUS316L nanoballs. O_2 and O^- most likely originated from the surface of SUS316L nanoballs, where MB molecules were attracted towards the surface because of the charge difference between the MB molecules and the SUS316L nanoballs surface. After oxidation into sulfoxide, photocatalysis process reduces sulfoxide into lighter products. At this stage, free radicals ($\cdot O$ and $\cdot OH$) attacked the bonds of MB and sulfoxide, severing the bonds, thus decomposing MB and sulfoxide into lighter products. Also, because MB decomposition showed two different pathways, it is supposed that there is a bottleneck effect between 6- and-24 hour UV-irradiation [23]. This effect caused the SUS316L nanoballs to react to different bonding sites in MB at different times.

In the case of TiO_2 and ZnO, O_2 has been consumed during the formation of the nanoballs from its parent materials, namely Ti and Zn. Therefore, no available O_2 existed for oxidation of MB into sulfoxide.

The results indicate a new discovery of MB decomposition pathway occurring in a non-semiconductor material, namely SUS316L nanoballs. Figure 4-9 shows the proposed mechanism of MB decomposition in 316L nanoballs. The reactivity of SUS316L nanoballs is due to its large surface area and reactivity of Fe_2O_3 and Cr_2O_3 as a light-sensitive material. Previous reports have shown that rust (which contained Fe_2O_3) acted as a photocatalytic material to accelerate the corrosion of stainless steel when exposed to sunlight, and that the passivation layer on the surface of stainless steel (which contained both Fe_2O_3 and Cr_2O_3) exhibited semiconductive behaviour [21-22]. Rust has the effect of acting as a photocatalytic material to enhance the corrosion of carbon steel [21]. The semiconductive behavior of passive films formed on stainless steel surfaces was also described [22].

Figure 4-10 shows the schematic diagram of the photocatalytic reaction occurring on the surface of a Fe_2O_3 nanoparticle.

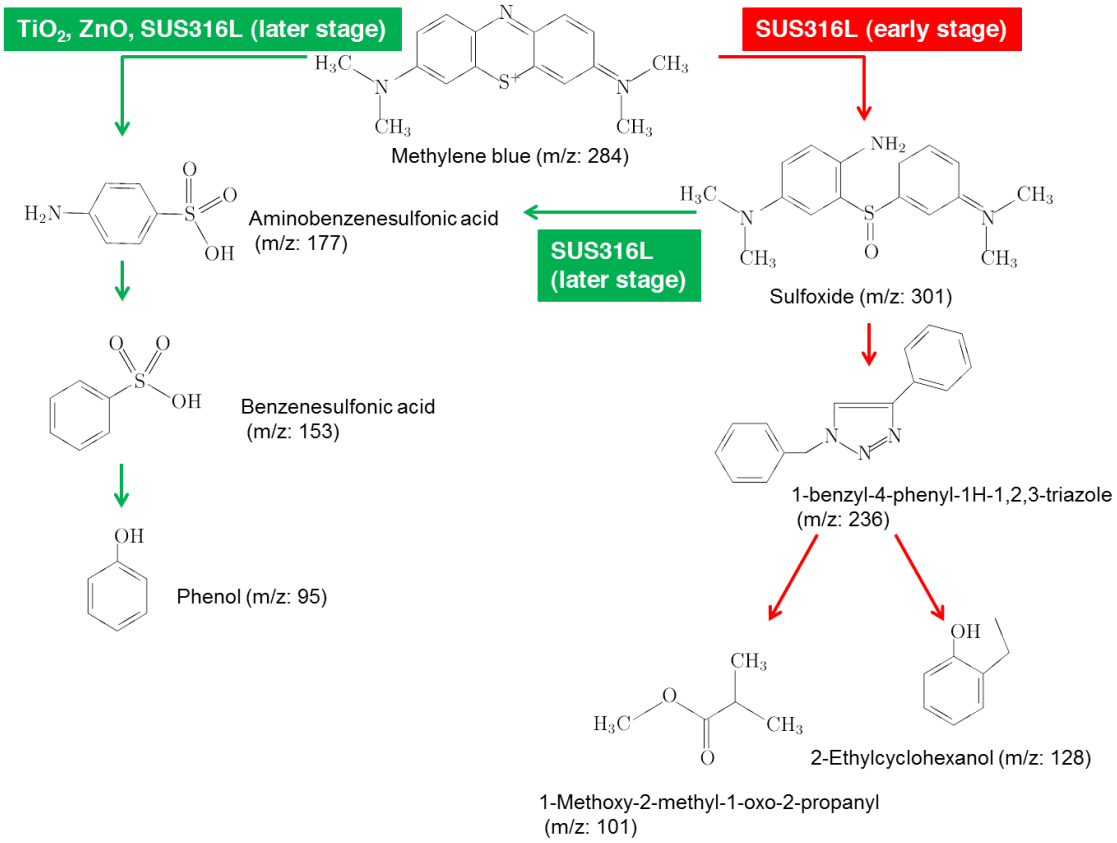

Figure 4-9 The proposed mechanism of MB photodecomposition in presence of SUS316L nanoballs showing the occurrence of fast and slow photodecomposition reaction.

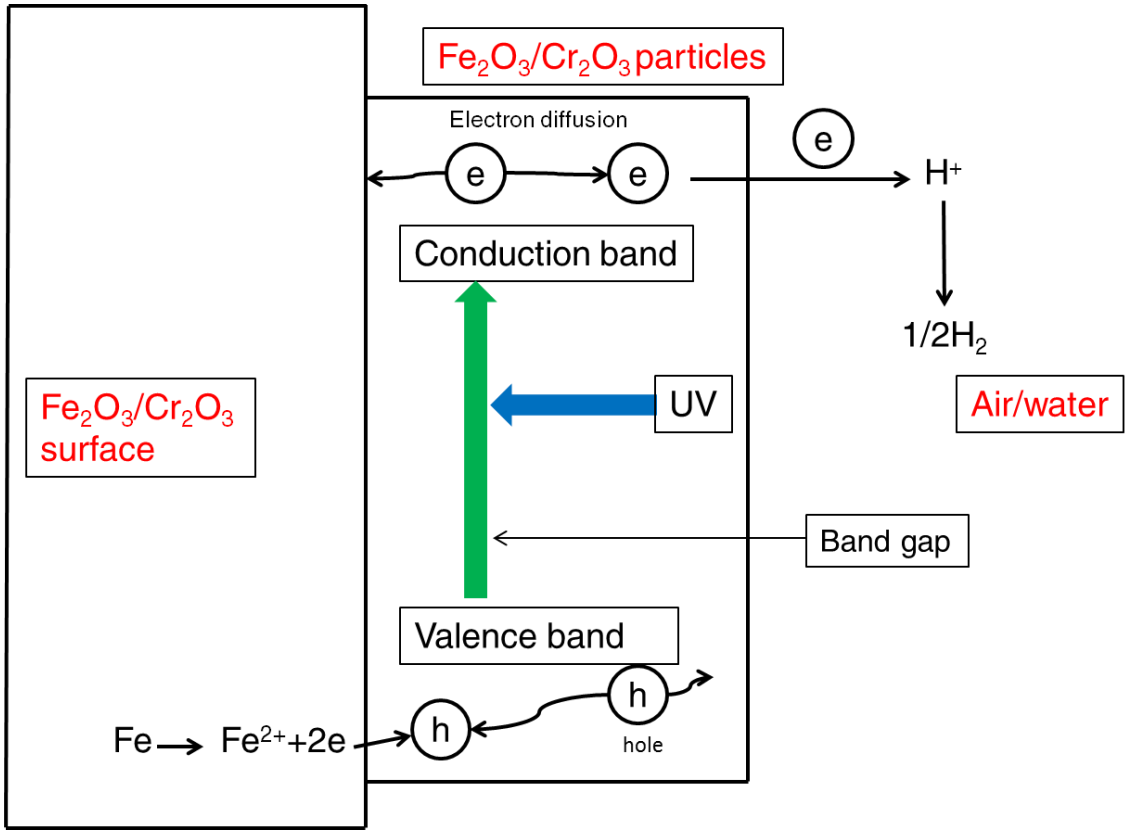

Figure 4-10 Schematic diagram of photocatalytic reaction occurring on the surface of a Fe_2O_3 nanoparticle.

4.5 Conclusions

In SUS316L nanoball case, MB decomposition occurred in two pathways; fast and slow decompositions. MB was observed to oxidise into sulphoxide before being reduced into lighter by-products. This is different compared to the MB decomposition pathway occurring in the presence of TiO_2 and ZnO nanoballs. In the case of TiO_2 and ZnO nanoballs, MB reduced into lighter by-products without being oxidised into sulphoxide first.

References

[1] A. I. Kozlov, A. P. Kozlova, H. Liu, Y. Iwasawa, Applied Catalysis A: General, **182** (1999) 9-28.
[2] K. J. Kim, H. G. Ahn, Applied Catalysis B: Environmental, **91** (2009) 308-318.
[3] K. Qian, J. Fang, W. Huang, B. He, Z. Jiang, Y. Ma, S. Wei, Journal of Molecular Catalysis A: Chemical, **320** (2010) 97-105.
[4] E. Kusiak-Nejman, M. Janus, B. Grzmil, A. W. Morawksi, Journal of Photochemistry and Photobiology A: Chemistry, **226** (2011) 68-72.
[5] E. E. Oguzie, G. N. Onuoha, A. I. Onuchukwu, Materials Chemistry and Physics, **89** (2005) 305-311.
[6] Z.D. Wei, F. Yin, L.L. Li, X.W. Wei, X.A. Liu, Journal of Electroanalytical Chemistry, **541** (2003) 185-191.
[7] S. Takenaka, A. Hirata, E. Tanabe, H. Matsune, M. Kishida, Journal of Catalysis, **274** (2010) 228–238.
[8] L. V. Mattos, F. B. Noronha, Journal of Power Sources, **145** (2005) 10-15.
[9] K. Imamura, E. Ikeda, T. Nagayasu, T. Sakiyama, K. Nakanishi, Journal of Colloid and Interface Science, **245** (2002) 50-57.
[10] C. Yogi, K. Kojjima, N. Wada, H. Tokumoto, T. Takai, T. Mizoguchi, H. Tamiaki, Thin Solid Films, **516** (2008) 5881-5884.
[11] R. Solarska, B.D. Alexander, A. Braun, R. Jurczakowski, G. Fortunato, M. Stiefel, T. Graule, J. Augustynski, Electrochimica Acta, **55** (2010) 7780-7787.
[12] A. Houas, H. Laccheb, M. Ksibi, E. Elaloui, C. Guillard, J-M. Herrmann, Applied Catalysis B: Environmental, **31** (2001) 145-157.
[13] K. L. Arvan, G. A Korsunovskii, Zhurnal Prikladnoi Spektroskopii, **4** (1971) 722-724.
[14] C. Noubactep, Journal of Hazardous Materials, **166** (2009) 79-87.
[15] C. H. Kwon, H. Shin, J. H. Kim, W. S. Choi, K. H. Yoon, Materials Chemistry and Physics, **86** (2004) 78-82.
[16] C. Liu, X. Tang, C. Mo, Z. Qiang, Journal of Solid State Chemistry, **181** (2008) 913-919.
[17] K. J. Hwang, J. W. Lee, W. G. Shim, H. D. Jang, S. I. Lee, S. J. Yoo, Advanced Powder Technology, **23** (2012) 414-418..

[18] S. Lakshmi, R. Reganathan, S. Fujita, Journal of Photochemistry and Photobiology A: Chemistry, **88** (1995), 163-167.
[19] N. Liu, G. Sun, Dyes and Pigments, **91** (2011) 215-224.
[20] S. Horikiri, N. Teshima, Y. Saruki, H. Nishikawa, T. Sakai, Bunseki Kagaku, **52** (2003) 881-885.
[21] M. Kumada, K. Shinoda, S. Kobuchi, K. Niwa, T. Yamada, Journal of Society of Materials Science Japan, **48** (1999) 1239-1243.
[22] H. Tsuchiya, S. Fujimoto, O. Chihara, T. Shibata, Electrochimica Acta, **47** (2002) 4357-4366.
[23] M. R. M bin Julaihi, S. Yatsu, M. Jeem, S. Watanabe, Journal of Experimental Nanoscience, (2014) DOI: 10.1080/17458080.2014.951408, 1-18.
[24] J. H. Baxendale, A. A. Khan, International Journal for Radiation Physics and Chemistry, **1** (1969) 11-24.
[25] S. Hisaindee, M. A. Meetani, M. A. Rauf, Trends in Analytical Chemistry, **49** (2013) 31-44.
[26] B. G. Kwon, S. Ryu, J. Yoon, Journal of Industrial Engineering Chemistry, **15** (2009) 809-812.
[27] L. Zang, P. Qu, J. Zhao, T. Shen, H. Hidaka, Journal of Molecular Catalysis A: Chemical, **120** (1997) 235-245.
[28] S. S. Shinde, C. H. Bhosale, K. Y. Rajpure, J. H. Lee, Journal of Photochemistry and Photobiology B: Biology, (2014) http://dx.doi.org/10.1016/j.jphotobiol.2014.10.015, 1-18.
[29] M. E. Simonsen, J. Muff, L. R. Bennedsen, K. P. Kowalski, E. G. Sogaard, Journal of Photochemistry and Photobiology A: Chemistry, **216** (2010) 244-249.
[30] B. Tryba, M.Toyoda, A. W. Morawski, R. Nonaka, M. Inagaki, Applied Catalysis B: Environmental, **71** (2007) 163-168.

Chapter 5 General Conclusions and Recommendations

Chapter 5 General Conclusions and recommendations

In general, this thesis is concerned with submerged glow-discharge plasma as a viable method to synthesize nanoparticles. The physical characteristics of the nanoballs were investigated. The nanoballs were found to have photocatalytic activity when irradiated with UV-light.

In Chapter 3, TiO_2, ZnO and SUS316L nanoballs were shown to be successfully synthesized via submerged glow-discharge plasma. The nanoballs were nanosized (10nm to 200nm in size) and uniformly spherical. Submerged glow-discharge plasma was demonstrated to be a simple, quick and inexpensive method to produce nanoballs with potential for scaling up for industrial use. Also, submerged glow-discharge plasma has the advantage of being able to synthesize multialloy nanoparticles.

In chapter 4, photoabsorbance showed that MB peak intensity was reduced by mixing with these nanoballs and UV-light irradiation. In all cases, absorbance peak of MB at 660nm became lower than initial height after UV-irradiation, which indicates decomposition of MB has occurred. It is considered that oxidization of MB is enhanced from early stage in case of TiO_2 and ZnO nanoballs.

However, in SUS316L nanoball case, more complex process with oxidation followed by reduction of MB was observed. This different compared to the process occurring in prescence of TiO_2 or ZnO nanoballs. SUS316L nanoballs included particles with and without oxide films; particles without oxide films are thought to be highly reactive.

During the synthesis of nanoballs, size control was achieved by modifying the glow discharge voltage. Higher glow-discharge voltage generally produced smaller sized nanoballs, while lower glow-discharge voltage produced larger sized nanoballs. This is shown in the case of TiO_2 and SUS316L nanoballs, where higher glow-discharge voltage produced small-sized nanoballs. For TiO_2, the maximum voltage that can be applied was 150 V, and for SUS316L 160 V. In the case of ZnO, voltages between 100 and 135 V produced flower-like nanoparticles, whereas the optimal voltage for spherical nanoball production was 95 V. However, there is a limit to the maximum voltage than can be applied; once this limit is exceeded, arc-discharge plasma appears and melts the electrode immediately.

There were relatively few microsized particles present after collecting the nanoballs. These are thought to be synthesised because of the irregularities of the plasma current flow.

There is a limit to the maximum voltage than can be applied; once this limit is exceeded arc-discharge plasma appears and melts the electrode immediately. There was also a risk of explosion occurring once the arc-discharge voltage is reached. Other than voltage control, the nanoballs can be separated according to size by using different-sized filters. Optimization of nanoballs' synthesis is needed to produce smaller sized nanoballs with larger surface area; BET measurement shows that the submerged glow-discharge has good potential to produce nanoballs with large surface area.

It is evident from the XRD and photoabsorbance results that only small amounts of Fe_2O_3 and Cr_2O_3 are present in SUS316L nanoballs. The small amount of photocatalytically active oxides in SUS316L nanoballs caused them to exhibit photocatalytic effect at a lower activity compared to TiO_2 and ZnO nanoballs. Further research is needed to increase the amount of those active species, thereby increasing the photocatalytic activity of SUS316L nanoballs. This potentially can be achieved either by decreasing their particle size or doping with other elements.

Acknowledgements

I would like to express my gratitude to Professor Seiichi Watanabe, Center for Advanced Research & Energy Conversion Materials of Hokkaido University. The work described in my thesis was conducted under his supervision. This research would not have been possible without his advices and encouragements. I would like to thank Assistant Professor Shigeo Yatsu for spending time with me doing valuable discussions and suggestions.

For assistance in the examination and improvement of my thesis, I would like to thank the members of the examination committee; Professor Kiyotaka Asakura and Professor Naoto Koshizaki. Their comments and advices allowed me to complete this thesis.

For experimental work, particularly for SEM and TEM observations I would like to thank Souki Yoshida and Dr, Junya Ishioka for their technical assistance and helpful suggestions. For XRD observations, I am indebted to Dr. Genki Saito for his assistance. The results interpretation might not be possible without their help.

I am also grateful to all members of the Watanabe Laboratory for their assistance in conducting the numerous experimental works. I would also like to give many thanks to the Malaysian students' community in Sapporo for their friendship and support throughout my stay here.

Finally, I would like to sincerely thank my parents Julaihi bin Bujang and Mazlin bt. Darus, younger brothers Izzat and Zakmal and Uncle Dan for their continuous moral support, humor and love.